Structure-dependent charge transfer at the interface between organic thin films, and metals and metal oxides

Sareh Ahmadi

Doctoral Thesis in Microelectronics and Applied Physics

Stockholm, Sweden 2013

Akademisk avhandling som med tillstånd av Kungl Tekniska högskolan framlägges till offentlig granskning för avläggande av teknologie doktorsexamen i Mikroelektronik och tillämpad fysik torsdagen den 12 december 2013, klockan 10.00 i Sal D, KTH-Forum, Isafjordsgatan 39, Kista, Stockholm.

Tryck: Universitetsservice US AB

Abstract

The purpose of the research work, presented in this thesis is to offer a detailed atomic level study of interfaces created by adsorption of organic molecules on metals and metal oxides to point out significant impact of substrate, dye structure as well as different mediators on the charge transfer at these interfaces, which is proven to influence the device performance to a great extent.

Adsorption of organic photosensitive molecules on metals and metal-oxides is the main focus of this thesis. Phthalocyanines which are organic semiconductors offer a broad range of properties, such as thermal and chemical stability, high charge mobility and strong absorption coefficient in the visible and near-IR regions, which make them very attractive to be applied in various systems and devices. Fuel cells, organic field-effect transistors (OFETs), organic light emitting diodes (OLEDs) and solar cells are examples of phthalocyanine's applications. The main focus of this work is to characterize the interfaces of Dye Sensitized Solar Cells (DSSCs). DSSC was invented by Michael Grätzel and Brian O'Regan in 1988. At the heart of this cell there is an oxide which is coated by a photosensitive dye. Under illumination, an electron is excited from HOMO to LUMO of the molecule, which can be further transferred to the conduction band of the oxide by a proper energy level alignment. The original state of the dye is regenerated by electron donation via the electrolyte, which usually is an organic solvent containing a redox couple e.g., iodide/triiodide. The iodide is regenerated by reduction of triiodide at the counter electrode. To improve the functionality of the cell, different additives can be added to the electrolyte.

To mimic the interfaces of this cell, molecular layers of MPc (M: Fe, Zn, Mg) are adsorbed on both metallic surfaces, Au(111) and Pt(111), and rutile $TiO_2(110)$. Layers of iodine were inserted between metallic substrates and dyes to investigate the electronic properties and charge transfer at these multi-interface systems. 4-tert-butyl pyridine is a significant additive to the electrolyte and has proven to enhance the cell's performance. This molecule was also adsorbed on Pt(111) and $TiO_2(110)$. Phthalocyanines were deposited by organic molecular beam deposition and 4TBP was evaporated at room temperature. Surface structures and reconstructions were confirmed by LEED measurements. Surface sensitive synchrotron radiation based spectroscopy methods, XPS and NEXAFS were applied to characterize these surfaces and interfaces. STM images directly give a topographical and electronic map over the surface. All measurements were carried out in UHV condition.

When MPc was adsorbed on Au(111) and $TiO_2(110)$, charge transfer from molecule to substrate is suggested, while the opposite holds for MPc adsorbed on Pt(111). Moreover, stronger interaction between MPc and Pt(111) and $TiO_2(110)$ compared to Au(111) also demonstrates the effect of substrate on the charge transfer at the interface. The stronger interaction observed for these two substrates disturbed the smooth growth of a monolayer; it also resulted in bending of the molecular plane. Interaction of MPc with metallic surfaces was modified by inserting iodine at the interface. Another substrate-related effect was observed when MgPc was adsorbed on $TiO_2(110)$; (1×1) and (1×2)-cross linked surfaces, where the surface reconstruction directly affect the molecular configuration as well as electronic structure at the interface. Besides, it is shown that the d-orbital filling of the central metal atom in MPc plays an important role for the properties of the molecular layer as well as charge transfer at the interface.

Upon adsorption of 4TBP on Pt(111), C-H bond is dissociatively broken and molecules is adsorbed with N atoms down. Modification of surface by iodine, prevent this dissociation. In the low coverage of iodine, there is a competition between 4TBP and iodine to directly bind to Pt(111). Investigation on the adsorption of 4TBP on $TiO_2(110)$ illustrated that these molecules in low coverage regime, prefer the oxygen vacancy sites and their adsorption on these sites, results in a downward band bending at the substrate's surface.

Keywords: photoelectron spectroscopy, X-ray absorption spectroscopy, organic semiconductors, phthalocyanine, charge transfer, electronic structure, dye sensitization.

Publications

List of papers included in this thesis

I. **Sareh Ahmadi**, Nina Shariati, Shun Yu and Mats Göthelid, "Molecular layers of ZnPc and FePc on Au(111) surface: Charge transfer and chemical interaction", *J. Chem. Phys.* 137 **(2012)** 084705

II. **Sareh Ahmadi**, Shun Yu, Markus Soldemo, Chenghua Sun and Mats Göthelid, "Reduced Au-MPc hole injection barrier by an intermediate iodine layer", Submitted to *J. Phys. Chem. C.*

III. **Sareh Ahmadi**, Björn Agnarsson, Ieva Bidermane, Bastian M. Wojek, Quentin Noel and Mats Göthelid, "Effect of the iodine on the site-dependent charge transfer at the Pt(111)-ZnPc interface", Submitted to *New J. Phys.*

IV. Shun Yu, **Sareh Ahmadi**, Chenghua Sun, Pooya Tabib Zadeh Adibi, Winnie Chow, Annette Pietzsch and Mats Göthelid, "Inhomogeneous charge transfer within monolayer zinc phthalocyanine adsorbed on TiO$_2$(110)", *J. Chem. Phys.* 136, **(2012)** 154703

V. **Sareh Ahmadi**, Shun Yu, Markus Soldemo, Marcelo Zuleta, Pål Palmgren and Mats Göthelid, "Charge transfer and band bending on TiO$_2$(110)-MgPc", Submitted to *J. Phys. Chem. C.*

VI. **Sareh Ahmadi**, Ieva Bidermane, Quentin Noel, Chenghua Sun and Mats Göthelid, "Dissociative bonding of 4-tert-butyl pyridine to Pt(111) and surface passivation by iodine", *manuscript.*

VII. Shun Yu, **Sareh Ahmadi**, Chenghua Sun, Pål Palmgren, Franz Hennies, Marcelo Zuleta, Mats Göthelid, "4-tert-butyl pyridine bond site and band bending on TiO$_2$(110)", *J. Phys. Chem. C*, 114, **(2010)**, 2315-2320

List of papers not included in this thesis

1) "Experimental and Theoretical Study of Electronic Structure of Lutetium bi-Phthalocyanine", Ieva Bidermane, Johann Lüder, Sophie Boudet, Teng Zhang, Sareh Ahmadi, Cesare Grazioli, Marcel Bouvet, Jan Rusz, Biplab Sanyal, Olle Eriksson, Barbara Brena, Carla Puglia, and Nadine Witkowski, J. Chem. Phys. **138**, (2013), 234701

2) "Photoelectron and Absorption Spectroscopy Studies of Metal-Free Phthalocyanine on Au(111) : Experiment and Theory "Masumeh-Nina Shariati, Johann Lüder, Ieva Bidermane,

Sareh Ahmadi, Emmanuelle Göthelid, Pål Palmgren, Sanyal, Biplab, Olle Eriksson, Maria Novella Piancastelli, Barbara Brena, Carla Puglia , J. Phys. Chem. C, **117** (2013),7018.

3) "Iodine structures on stepped Pt surfaces", Sareh Ahmadi, Shun Yu, Dunja Stoltz, P. Tabib Zadeh Adibi, J. Adell, Mats Göthelid, manuscript

4) "Electronic structure of ordered iodine layers on Au(111), Pt(111) and Cu(111)", Sareh Ahmadi, Shun Yu, Mats Leandersson, Dunja Stoltz and Mats Göthelid, in preparation

5) "Structure, adsorption energy, charge density and chemical reactions in iodine layers on Pd(111)", Benjamin. Bruhn, Sareh Ahmadi, Pål Palmgren, Henrik. von Schenck, Jonas Weissenrieder, Mats. Göthelid, and Chenghua Sun, Submitted to J. Phys.Chem.

6) "Adsorption of TiOPc on (1x1) and (1x2) reconstructed rutile TiO$_2$(110) surfaces", Shun Yu, Sareh Ahmadi, Pål Palmgren, Franz Hennies, Anneli Önsten, Mats Göthelid, manuscript

7) "Surface concentration dependent structures of iodine on Pd(110)", Mats Göthelid, Michael Tymczenko, Winnie Chow, Sareh Ahmadi, Shun Yu, Benjamin Bruhn, Dunja Stoltz, Henrik von Schenck, Jonas Weissenrieder, and Chenghua Sun, J. Chem. Phys. **137** (2012), 204703

8) "Light-induced rearrangements of chemisorbed dyes on anatase(101)", Marcelo Zuleta, Tomas Edvinsson, Shun Yu, Sareh Ahmadi, Gerrit Boschloo, Mats Göthelid, Anders Hagfeldt, Phys. Chem. Chem. Phys. **14**, (2012) 10780

9) "Crystallization Induced Charge Transfer in TiOPc Thin Films Revealed by Resonant Photoemission Spectroscopy" Shun Yu, Sareh Ahmadi, Marcelo Zuleta, Karina Schulte, Annette Pietzsch, Franz Hennies and Mats Göthelid, J. Phys. Chem. C **115** (2011) 14969

10) Structure dependent 4-tert-butyl pyridine induced band bending at TiO$_2$ surfaces", Mats Göthelid, Shun Yu, Sareh Ahmadi, Chenghua Sun, Marcelo Zuleta, J. Photoenergy. (2011)

11) "Adsorption Geometry, Molecular Interaction and Charge Transfer of Triphenylamine-based Dye on Rutile TiO$_2$(110)", Shun Yu, Sareh Ahmadi, Marcelo Zuleta, Haining Tian, Karina Schulte, Annette Pietzsch, Franz Hennies, Jonas Weissenrieder, Xichuan Yang and Mats Göthelid, J. Chem. Phys. **133** (2010) 224704

12) "Monitoring N719-dye Configurations on (1xn)-Reconstructed Anatase (100) by means of STM: Reversible Configurational Changes upon illumination", Marcelo Zuleta, Shun Yu, Sareh Ahmadi, Gerrit Boschloo, Mats Göthelid and Anders Hagfeldt, Langmuir **26** (2010) 13236

13) "Modification of Charge Transfer and Energy Level Alignment at Organic/TiO$_2$ Interfaces", Shun Yu, Sareh Ahmadi, Pål Palmgren, Franz Hennies, Marcelo Zuleta, Mats Göthelid, J. Phys. Chem. C **113** (2009) 13765

Acknowledgements

In the fall 2006 I took a course during the first year of my master studies, which somehow changed my study path and to some extent my life. The course was called "Experimental Techniques – Surface". The course was very interesting and advanced. The time was a bit short and I was not used to 7-week periods at KTH yet, but I got lots of motivations and inspirations from the person who was teaching with so much passion about his research field. I received the top grade in that course and on top of that I was offered to do my master thesis on the same topic, "surface science". Today I am very glad that I passed that course, got a good grade, and accepted the offer to do my master thesis and following that got admitted to do my doctoral studies at the group of Prof. Mats Götelid. There are too many things that I should thank you for. For your endless patience, great understanding of the different situations, positive attitude, and being a great teacher. I have learned a lot from you; most importantly I have learnt how to learn better. I was very lucky to work together with a competent experimentalist person, who always has great ideas.

My great gratitude to Prof. Oscar Tjernberg, my official supervisor and head of the unit, who was a great support for me during my studies, and helped me with both scientific issues and administrative issues. I am very grateful.

I would also like to thank Prof. Ulf Karlsson, my co-supervisor and head of the Material's platform for his support during the years that I was at Material Physics. I deeply admire your ideas and efforts to promote science. What you are doing is very valuable and many scientist, now and in the future will benefit from that. It has always been a pleasure to listen to your talks, whether you talk about the new synchrotron radiation source or skiing or travelling, you add a great deal of good spirit to it. You asked me a few times how my Swedish is and maybe I have disappointed you, så jag säger det här på svenska: tack så mycket för åren på Materialfysik.

I would like to express my gratitude to Dr. Shun Yu, my colleague for more than four years. You helped me a lot in finding my way in the laboratory, working with vacuum systems and sample preparations. I sincerely thank you for all the help and support during the experiments in Kista, our long and challenging beamtimes at MAX-lab and for scientific discussions. I learned a lot from you and with you. You are a hardworking, smart, young scientist and I hope you keep moving up toward your dreams.

I also express my gratitude to my colleagues at the surface physics group. Dr. Anneli Önsten, you are a great colleague and a great friend. I'm very grateful for your kindness and your support during these years. Many thanks to Dr. Pål Palmgren, Dr. Marcelo Zuleta, Dr. Dunja Stoltz, Dr. Winnie Chow, Dr. Michael Tymczenko, A. Prof. Jonas Weissenrieder and Markus Soldemo for experimental work and fruitful discussions over the years.

Contents

Chapter 1

Introduction

The research work presented in this thesis is focused on adsorption of phthalocyanines on metallic surfaces, modified metallic surfaces, as well as TiO_2. Besides, adsorption of small metal-free organics is investigated on both metallic and oxide surfaces.

Phthalocyanines have similarities with naturally occurring porphyrins, chlorophyll and hemoglobin, which are involved in important biological processes of photosynthesis in plants and oxygen transport within the red-blood cells[1–3]. This fact was the origin of interest in phthalocyanines, since they could be used as models for biological systems. These macro-cyclic compounds are conventionally used as dyes and pigments. However their applications have been growing much broader in recent years. The properties such as thermal and chemical stability, conductivity (their HOMO-LUMO gap is comparable with inorganic semiconductors), long diffusion length of charge carriers, high charge mobility and strong absorption coefficient in the visible and near-IR regions make them attractive for use in various systems and devices. These characteristics make them promising candidates to be used in catalysis[2], fuel cells[4–6], organic thin-film transistors[7], organic field-effect transistors (OFETs)[8], organic light emitting diodes (OLEDs)[9–11] , photodynamic cancer therapy[12,13], sensors[14,15], and dye sensitized solar cells[7,16–18].

The function of these devices is influenced by an essential factor; interaction and charge transfer at the interface between Pc and the substrate. Numerous studies, applying several experimental and theoretical methods have been carried out to investigate the interfacial interaction and charge transfer, as well as the effect of these interactions on the functionality of devices. Charge transfer at the interface of Pc and substrate can determine the layer growth mode, molecular configuration, magnetic properties, optical properties and charge injection, which would effectively modify the organic device function. This has encouraged many research groups to investigate the effect of substrate-adsorbate interaction on the properties of the molecular layer and consequently the potential devices, which would have organic components of similar nature[19–34].

Besides, manipulation of the interaction at the interface of MPc-substrate is possible by either decorating the molecules (adding external atoms or molecules to the center or periphery of Pcs)[35–37] or modifying the substrate by inserting an intermediate layer[38,39]. Adsorption of other molecules on top of

Pc thin films has been also reported[40–44]. For instance, upon adsorption of pyridine on an ordered monolayer of FePc on Au(111), pyridine molecules coordinate to the iron site. This coordination led to a strong ligand field which modified the magnetic and electronic properties of the iron atom[42]. In another study, Gerlach, et.al.[37] showed that by fluorination of CuPc adsorbed on Cu(111) and Ag(111), the molecular distortion and interfacial interactions are modified.

The work presented in this thesis is mainly focused on the application of phthalocyanines in dye sensitized solar cells (DSSCs). At the heart of the DSSC, there is a mesoporous oxide layer, which can be TiO_2, ZnO or Nb_2O_5. The oxide is coated by dye molecules for sensitization. Under illumination, an electron is excited from HOMO to LUMO of the molecule and with a proper energy level alignment this electron can be transferred to the conduction band of the oxide. The original state of the dye is restored by electron donation via electrolyte, usually an organic solvent containing a redox couple e.g., iodide/triiodide couple. The iodide is regenerated by reduction of triiodide at the counter electrode. In order to improve the device performance, different additives have been introduced to the electrolyte[45]. One important additive is 4-tert-butyl pyridine (4TBP), which increased the fill factor and the open circuit voltage by approximately 0.4 V[46].

In this thesis, adsorption of FePc and ZnPc on Au(111) and ordered Au(111)-I surfaces (section 3.2.1) are studied in paper I and paper II, which discuss the effect of central metal atom of MPc on its interaction with the substrate, as well as the influence of the substrate modification. In paper III, ZnPc is adsorbed on Pt(111), where molecules experience a stronger interaction with the substrate than on Au and this interaction is further modified by adsorption of ZnPc on ordered Pt(111)-I (section 3.2.2). Introducing iodine as an intermediate layer was done to mimic the electrode/electrolyte/dye multi-interface. TiO_2 is used as substrate in paper IV and paper V, where adsorption of ZnPc and was studied. Paper VI and paper VII discuss the effect of 4TBP, the additive in the electrolyte, on both Pt(111) and TiO_2 surfaces respectively. In paper VI, the effect of iodine as intermediate layer between Pt and 4TBP on the electronic structure at the interface as well as molecular configuration is investigated.

All the measurements in this work were done on single crystal substrates to eliminate the effects from different planes and reduce defects to a controlled amount. Instead of larger molecules, which have shown higher efficiency in DSSCs, phthalocyanines with lower measured efficiency are used, which are smaller compared to for instance ruthenium complexes and enable us to carry out a detailed atomic-level study on their interface with different substrates. Moreover, to better control the measurement conditions, experiments are done in ultrahigh vacuum (UHV) chambers. Surface sensitive methods, XPS, XAS and STM are used to characterize the surface properties. The spectroscopy measurements are performed at the MAX lab synchrotron radiation facility. These facilities provide high performance light sources, enabling high-resolution measurements.

The main goal of this thesis is to provide a detailed molecular description of reactions, structure and charge transfer at interfaces in organic photovoltaics, applying highly advanced characterization and

preparation methods. The relation between charge transport in a thin film and its structural properties is also elucidated. This thesis has taken the initial steps to study a model-system for organic photovoltaics, applying surface science characterization methods. On the basis of the discussions presented in this work, further modifications or replacements of different components can be carried out to improve the performance of this type of solar cells.

Chapter 2

Experimental Methods

2.1: Synchrotron Radiation

Synchrotron radiation is used as light source for a large number of experimental techniques. Great advantages such as high photon flux, high brilliance (Brilliance: number of photons/(time × spot size× convergence × 0.1% band width), tunable photon energy, linear polarization, pulsed time structure and wide range of energy provided by synchrotron radiation sources, make them the most versatile light sources available.

The basic principle behind it is based on an electromagnetic theory, in which when a charge is accelerated, it radiates. In a synchrotron radiation source, electrons are confined in a storage ring by means of magnetic fields. When electrons are accelerated in a circular path with relativistic velocity, a cone-shaped radiation will be emitted offering a wide spectral range, from IR to X-rays.

To be more specific, a storage ring is not perfectly circular but rather polygon and the straight sections are connected to each other by vacuum pipes with an angle. The electrons are bent in the ring mainly by bending magnets, which are pairs of big magnets. In the straight sections of 3rd generation storage rings, insertion devices such as wigglers and undulators are also installed to enhance the brilliance. These insertion devices have rather similar structures, both comprising of a periodic magnet array. However the magnetic field applied in a wiggler is stronger than the one for the undulator, which results in higher energies and a continuous spectrum as well as larger divergence than from an undulator (See Figure 2-1). To maximize the intensity of the photon energy coming out of the undulator, the undulator gap should be adjusted properly.

The generated light in the storage ring will be conducted to the beamlines with experimental equipment besides the monochromator and focusing components. The experiments in this work are mostly done at beamline I-511 (hv: 100 eV-1500 eV) which is an undulator-based beamline for UHV surface science research. Some of the experiments are completed at the beamline D-1011 (hv: 30 eV-1600 eV) which is a bending magnet beamline.
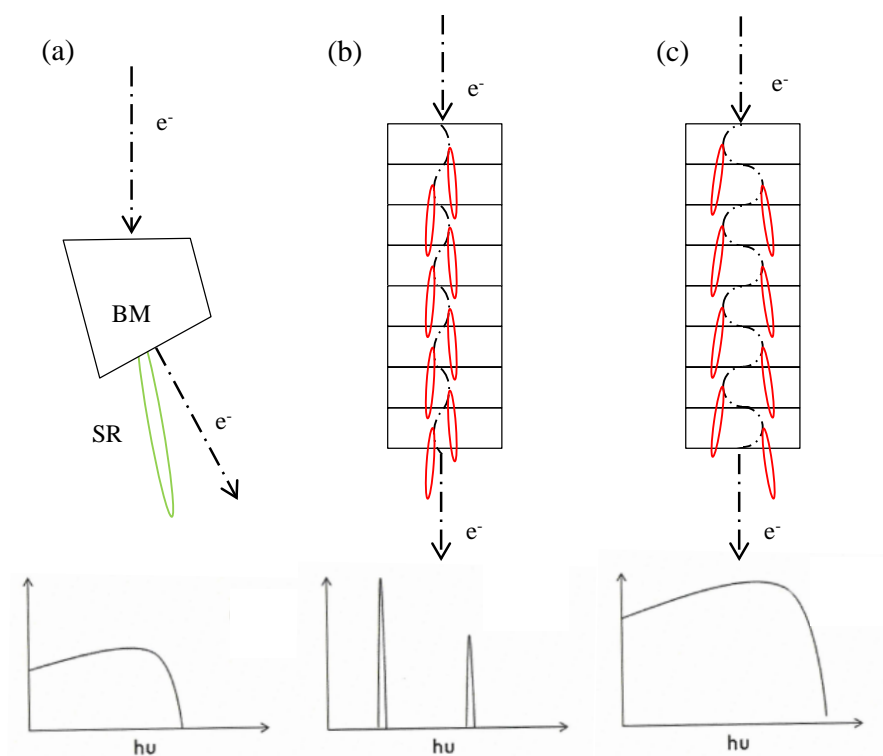
Figure 2-1: Schematics of the electron trajectories and the photon spectrum generated by in **(a)** bending magnet, **(b)** undulator and **(c)** wiggler.

2.2: Spectroscopy Techniques

2.2.1. X-ray Photoemission Spectroscopy

Photoelectron spectroscopy (PES) is a powerful experimental technique that provides information about the occupied electronic states of molecules or solids. This technique is based on the photoelectric effect which was discovered by Heinrich Hertz in 1887 and later explained theoretically by Albert Einstein that the photon energy depends on the frequency of the light rather than the intensity.

Electrons in materials can be excited to higher energy levels upon exposure to the light. When photons hit the material, electrons absorb the photons and if the incident photon has high enough energy, these electrons (photoelectrons) overcome the material's energy barrier (work function) and enter the vacuum (continuum state). A schematic view of the photoemission process is shown in Figure 2-2.
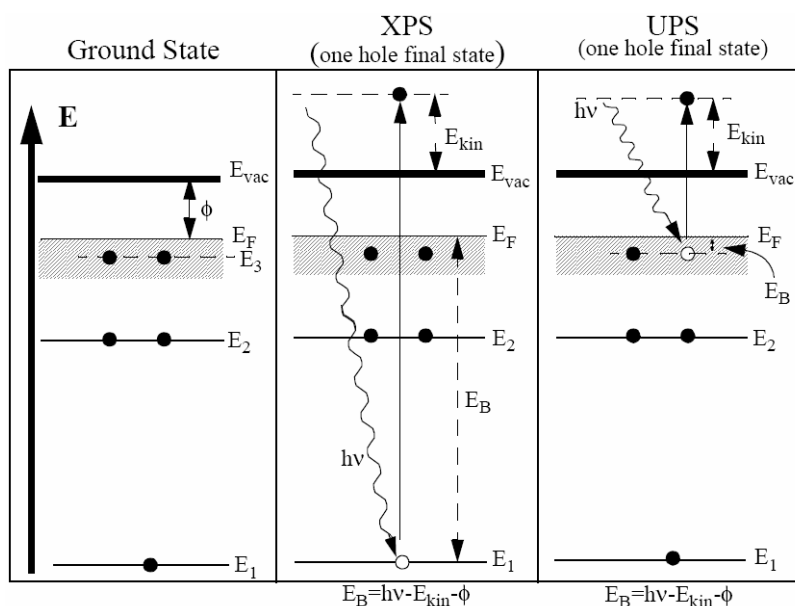
Figure 2-2: The photoemission process (XPS and UPS). In core level photoemission by illumination of photon of proper energy, a core electron is excited above the vacuum level. In UPS, the radiated photon lifts an electron from the valence band to the continuum.

When applying photons with a well-defined energy hv, intensity of the emitted photoelectrons is measured as a function of kinetic energy (KE) using an electron energy analyzer (electron spectrometer). The binding energy (E_B) of the photoelectron is then determined by the energy conservation law (equation 2.1), where Φ represents work function of the sample (energy difference between Fermi level and vacuum level)[47].

$$KE = hv - E_B - \Phi \quad (2.1)$$

The technique was developed by Prof. Kai Siegbahn in the 1950's and was called Electron spectroscopy for chemical analysis (ESCA) and later denoted X-ray Photoelectron Spectroscopy (XPS)[48]. This technique is used to study the electronic structure, chemical composition and chemical bonds of molecules and solids.

The photoelectron which found its way out of the sample's surface is then collected by the photoelectron spectrometer. A schematic of the hemispherical analyzer is shown in Figure 2.3. There are retarding lenses at the entrance, which are used to adjust the incoming photoelectrons to the defined pass energy. The photoelectron then enters the hemispherical electrodes. The concentric hemispherical analyzer (CHA) possesses double layer structure electrodes, where inner and outer shells have different electrical potentials. These electrodes only conduct electrons with the desired kinetic energy to a micro-channel-plate (MCP) at the end of trajectory. The signal is enhanced using cascade amplifiers. A large number of electrons hit the phosphorescence screen and the signal will be recorded on a charge-coupled-device (CCD) camera. Electrons with higher or lower kinetic energy than the pass energy collide with the electrodes.
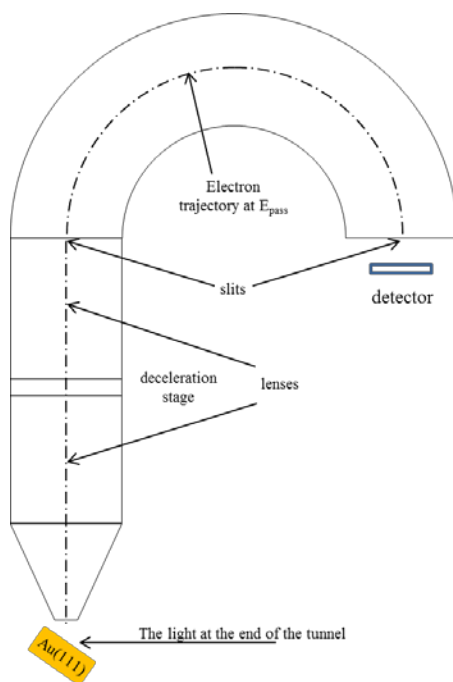
Figure 0-3: The schematic view of the hemispherical electron energy analyzer.

Photoelectron spectroscopy is classified as X-ray photoelectron spectroscopy (XPS) and Ultraviolet photoelectron spectroscopy (UPS), depending on the incident photon energy. However, since nowadays synchrotron sources allow us to choose the photon energy in a wide and continuous range of energies from UV to soft x-ray, the border between these two photoemission spectroscopies is not explicit.

Cross section

As mentioned above, even though synchrotron facilities give us the opportunity to select any photon energy from the spectrum of a fairly large window, one should keep in mind photon-electron interaction cross-section in order to choose the proper photon energy. Electrons from the same orbital can be excited with different quantum efficiencies depending on the photon energy, which makes it important to consider this fact while selecting the photon energy for measurements. A complete set of the cross section for 103 atoms at different photon energies are published by Yeh and Lindau[49], guiding us to choose the proper photon energy to probe the molecular orbitals.

Mean free path

Another point which one has to consider, when selecting a photon energy for photoemission experiments is the scattering of the electron inside the matter. The excited electron can be inelastically scattered by phonons or plasmon excitations. X-rays can penetrate deep in to solids (µm range), but actually the detected photoelectron in the photoemission experiments come from the topmost atomic layers, since the interaction with the matter is much stronger. From the electrons which reach the

analyzer, only the elastically scattered ones will contribute to the main peak of the photoemission spectrum. The distance an electron can travel inside the matter without experiencing inelastic scattering is called "mean free path". This distance is defined more by the kinetic energy of the electron rather than the type of matter. In fact since the average length that an electron travels will be reduced by elastic scattering processes, and consequently probability of inelastic losses become higher, the kinetic energy of the excited electron plays an important role, determining this travel distance. The mean free path versus kinetic energy curve is given in Figure 2.4 and shows the surface sensitive energy range. This curve which is called the "universal curve" exhibits that electrons with kinetic energy between 50 to 100 eV show the minimum mean free path, and electrons with kinetic energy higher or lower than this kinetic energy, have larger probe depth. This decreases the surface sensitivity. By increasing the thickness of the upper layer, intensity of the substrate declines exponentially.
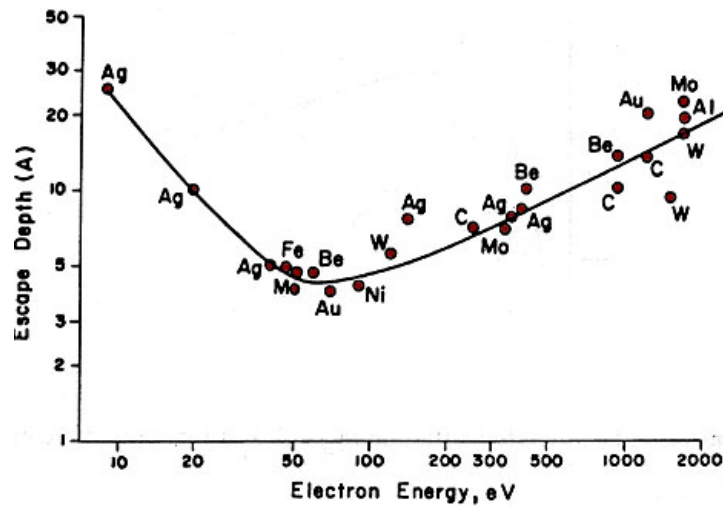
Figure 2-4: Mean free path of electrons at various kinetic energies[50].

Therefore, surface sensitivity can be used to calibrate the coverage of a thin film as shown in equation (2.2), where I_d is the intensity collected at the surface, I_0 is the intensity from the depth d and λ is the inelastic mean free path.

$$I_d = I_0 \exp(-d/\lambda) \ (2.2)$$

Emission angle

Besides the kinetic energy, the emission angle also affects the surface sensitivity. Two different commonly used emission angles (normal and grazing emission) are depicted in Figure 2.6. Going from normal emission to grazing emission, the photoelectron has to travel longer to reach the vacuum and escape the surface, which would cause higher probability of inelastic scattering for the excited electron from some depth, letting only the surface-area electrons make it out of the surface and reach the analyzer.
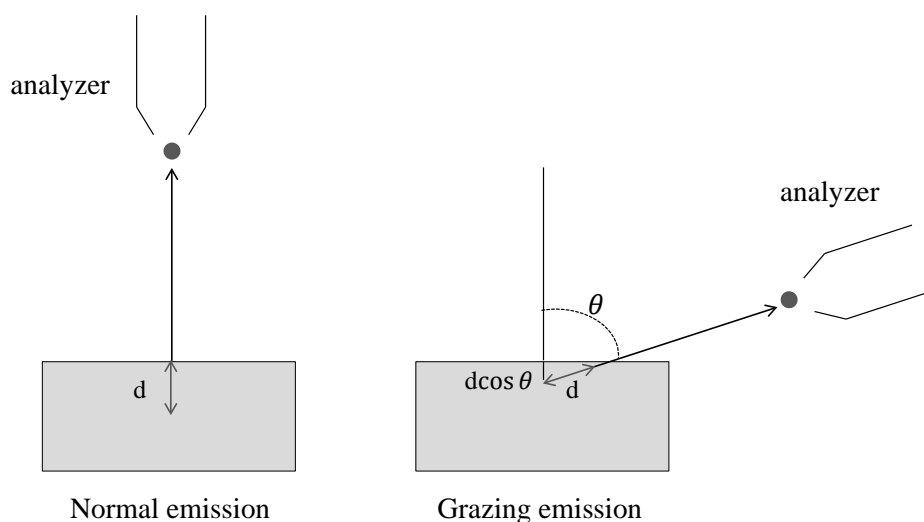
Figure 2.5: illustration of increasing the surface sensitivity in photoemission experiments, by going from normal emission to grazing emission. Mean free path (d) is the same in both cases; however in grazing emission the probe depth is smaller than in normal emission, which results in higher surface sensitivity achieved in grazing emission.

XP spectrum

In an x-ray photoelectron spectrum, the number of collected electrons as a function of binding energy is displayed (Figure 2.6.). The electron binding energies are element-specific and specific for each particular level inside an atom. Even though core electrons are localized and do not participate in chemical bonds, they will be influenced by any variation in the charge distribution of valence bands. These variations can be due to initial or final state effects and can give a shift (called chemical shift) to the core-level spectra. Initial state effects are the shifts which are related to the ground state system and are caused by electron-density-induced binding-energy changes. On the other hand final state effects appear in the core-excited state of the system; when an electron leaves the matter, screening of the core hole and refilling induce changes in the spectrum which are considered as final state effects. The origin of chemical shifts is the surrounding electronic environment and neighboring atoms. In other words, an electron rich environment shifts the core level to lower BE, whereas a low electron density environment shifts the core level to higher BE.

But before making further interpretation of XPS results, an energy calibration should be done. For solid systems, the zero energy is chosen at the Femi level. For metallic substrates, Fermi level is measured directly on the sample, though for the semiconductor sample it had to be measured on a metallic (Tantalum) foil in direct electrical contact with the substrate.
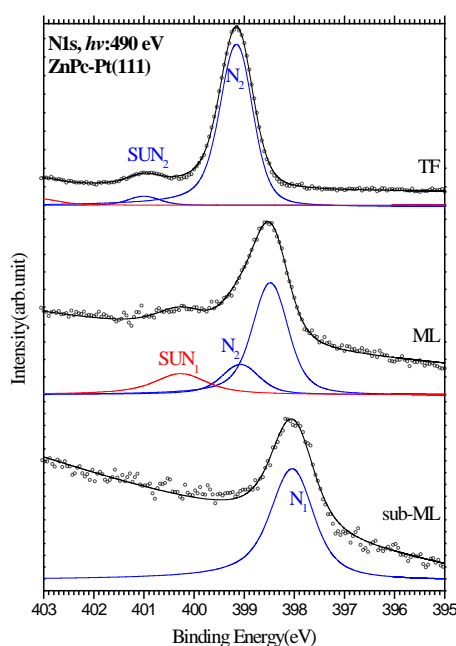
Figure 2.6: N1s spectra of ZnPc on Pt(111). From bottom to top: sub monolayer of ZnPc, monolayer and the thick film. The shift between N_1 of the sub-ML and N_2 of the TF is a final state effect. N_1 and N_2 are the two chemically shifted spectra, corresponding to the molecules at the first and second layer on Pt respectively. SUN_1 and SUN_2 are the shake-up structures.

Resolution

Another concept to be considered for an XP spectrum is the resolution. The parameters affecting the resolution give two types of peak broadening; the first group gives a Gaussian broadening to the peak. Mostly external parameters such as light source, optical components and detector contribute to the Gaussian width, but phonon excitations and different chemical components can also affect the Gaussian width. The second group contributes to the Lorentzian width, which corresponds to the core-hole lifetime. In some cases curve-fitting applying Voigt (Gaussian-Lorentzian) functions should be done, in order to distinguish the different contributions. For example, in case where the shift between different chemical components is not easily resolved in the spectrum, by curve-fitting one can deconvolute the different peaks, which can give invaluable information about the studied system. An example is presented in Figure 2.6, showing two different N1s peaks of Zinc Phthalocyanine adsorbed on Pt(111), which are chemically shifted with respect to each other due to different interaction with the substrate.

In a spectrum such as the ML in Figure 2.6, different relative intensities for different peaks are observed, which simply correlate with the number of each atom. However diffraction effects[22] and photoionization cross-section issues can vary the ratio between the different peaks.

Satellites

Additional features at higher binding energy of the main peak of the photoelectron spectrum are often observed. These features which are called satellites, appear when an excitation in the molecular valence levels takes place at the same time as the photoelectron is ejected. If the valence electrons are excited to bound states, the satellite is called shake-up. This secondary excitation in semiconductors appears as an extra peak and since this excitation reduces the photoelectron kinetic energy, the additional peak appears at the higher binding energy than the main peak. In semiconductors, the minimum energy an electron in the valence band needs to be excited to the conduction band is equal to the band gap. The difference in the binding energy of this shift peak corresponds to the band gap of the semiconductor. In the organic semiconductors, the observed shake-up structure is the consequence of excitation of an electron from HOMO (Highest Occupied Molecular Orbital) to LUMO (Lowest Unoccupied Molecular Orbital) of the molecule, and the shift from the main peak is equal to the HOMO-LUMO gap[51]. If the photoelectron is emitted to vacuum, similar to shake-up there will be a satellite which is described as a shake-off. The shake-off structures appear in higher binding energies than shake-ups[47].

In metals, instead of an additional peak, a difference in the photoelectron spectrum's line-shape is observed. Upon exciting an electron from the valence band of the metal surface to its conduction band, while the photoelectron is emitted, a reduction in the photoelectron kinetic energy takes place. This reduction in the photoelectron's kinetic energy gives rise to intensity on the low-kinetic energy side which is translated to be the high-binding energy side. Therefore, when fitting the spectra from metallic surfaces, an asymmetry factor has to be considered, which gives a "Doniach-Sunjic" line shape.

2.2.2. X-ray Absorption Spectroscopy

X-ray absorption spectroscopy (XAS) also known as "near edge x-ray absorption fine structure" (NEXAFS) is another surface sensitive method which is applied to study the electronic structure of the empty states (unoccupied orbitals in molecules and conduction band in solids). The absorption process is shown in Figure 2.7 schematically. This technique deals with structure up to 30 eV above the absorption edge.
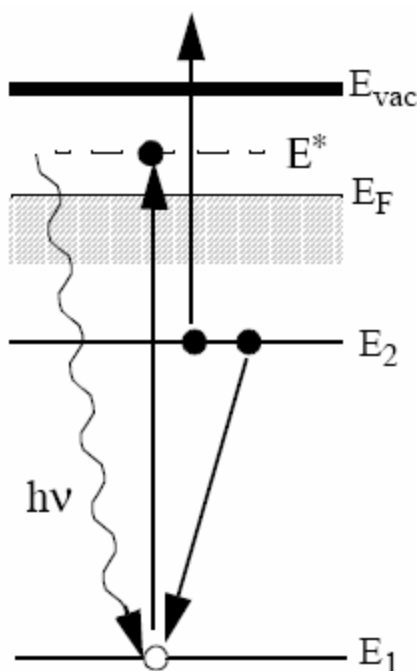
Figure 2.7: Schematic representation of the x-ray absorption process.

In this method, an X-ray photon is absorbed as its energy is scanned through the absorption edge. Since the photon energy needs to be scanned continuously, these types of measurements require a tunable source in a relatively large energy window, and synchrotron radiation is the solution for it. Once the incident photon is of sufficient energy, it can lift the core electron to an unoccupied state, which leaves the sample in an unstable situation. But this core hole will be filled by another electron, either radiatively by fluorescence decay or non-radiatively via Auger decay. The screening of the created core hole is done within femto- to attoseconds time frame. The final state of the XAS is the main difference between this method and XPS, since XAS possess a "self-screened" final state. In XPS, since the photoelectron leaves the sample and enters the vacuum, screening has to be done by the surrounding electronic environment. The significant experimental characterization of XAS is the ability to map the unoccupied states, whereas XPS provides the information of the occupied states. Besides, both methods are element specific and also chemically specific (responds differently to different electronic environment of the same atom); hence these two methods, as complementary methods to each other can deliver broad and detailed information about different electronic states of the studied system.

Different methods can be used to detect and record an XA spectrum, depending on the equipment and the field of research. These possible methods are: transmission, fluorescence and Auger decay. Transmission is when the intensity of transmitted X-ray is measured before and after the sample. This seems to be a straightforward technique; however it requires a very thin solid film. It can also be used in the measurement on liquids due to their higher penetration depth with respect to solid matters. Fluorescence decay can be measured by a fluorescence detector but the dominant decay, following K

edge excitations for low-Z elements (Z: atomic number) is Auger decay, since typically in an absorption process, both Auger processes and photoemission processes take place (Auger peaks are recognized by their fixed kinetic energy). Therefore since in this work K edge of N and C are measured, we have used Auger decay methods.

Auger decay methods are classified in three categories. First one is Total Electron Yield (TEY) which has contribution from both elastically- and inelastically-scattered electrons. Since inelastically scattered electrons bring information from a deeper region, this method is mostly used for bulk studies. By applying a retarding voltage in Partial yield method and filtering the low kinetic energy electrons, surface sensitivity is enhanced. The third method based on Auger decay is the Auger electron yield (AEY) which is somehow different from the first two. In this case, we use the photoelectron spectrometer to detect the electrons, since this would make it possible to measure constant-kinetic-energy Auger electrons. This kinetic energy is the kinetic energy of the desired Auger peak, and the photon energy range normally starts just below the absorption edge. Number of Auger electrons (intensity) depends on the number of excited electrons, and that itself depend on the absorption cross-section. This method (AEY) provides the most surface sensitive detection technique. In this thesis, the XAS data are collected with both TEY (at the beamline D-1011, MAX lab) and AEY (at the former beamline I-511, MAX lab).

Intensity of the recorded spectrum might have contributions from the light intensity correlated with the incident photon energy and continuous movement of monochromator and insertion devices while scanning the photon energy. It also might be influenced by the contamination of the optical components along the beamline. Therefore it is necessary to calibrate the intensity by recording the photocurrent at the gold mesh just in front of the sample and dividing the XAS data to this recorded current. To remove the contributions of contaminations, the spectrum can be normalized to the spectrum recorded from the clean substrate. In this way the useful data will be separated from contributions of the background. Not only the photon intensities, but also their energy should be calibrated. This is done by measuring the kinetic energy of a core level with the first and second order light, keeping the monochromator fixed. The difference in the measured energy gives the actual photon energy.

The first resonance in the spectrum, as shown in the Figure 2-8 represents the transition from the core level to the lowest unoccupied molecular orbital (LUMO) typically a π^* and the broad peak at higher photon energy corresponds to the transition from the core level to σ^* states. The system is perturbed upon XAS. This affects the resonance peaks in the XA spectrum. π^* states which are located just below or above the vacuum level, can be shifted all the way down below the Fermi level and for the first resonance peak, it might even be lower than the binding energy of the same core level binding energy measured by photoemission. This shift to lower energy is described by the Coulomb potential between core-hole and the excited electron. However delocalized weakly-bound σ^* states are located

above the vacuum level. This causes a shorter lifetime for the excited electron in comparison with the one excited to π^* and this short lifetime leads to broadening of the peak.
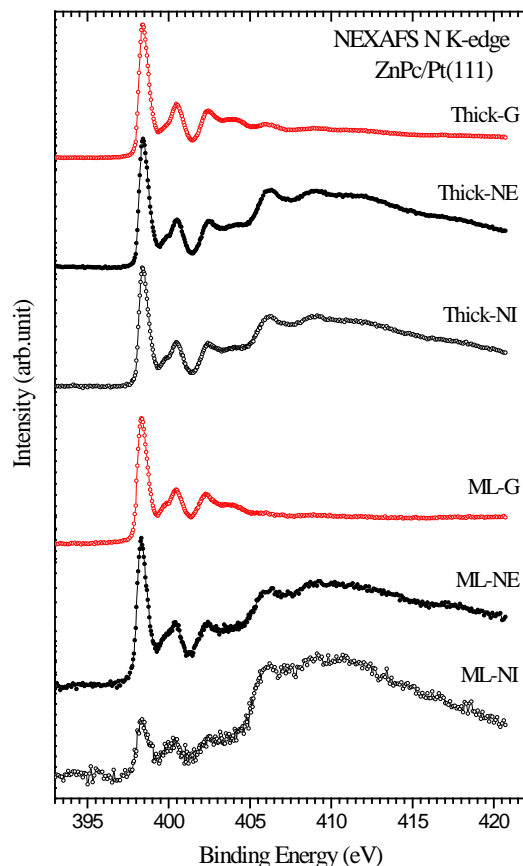
Figure 2-8: N K-edge XAS of a monolayer and a thick film of ZnPc on Pt(111), showing that ZnPc molecules are almost flat in the ML regime, but tilted at the TF.

One of the significant points about XAS is that it enables us to determine the orientation of the adsorbed molecules with respect to the substrate. Intensity of resonances in XA spectra is directly proportional to the absorption cross-section, which is highly angular dependent. As a consequence of this, the angle between the light polarization and the molecular orbital influences the intensity of that resonance peak. In Figure 2-9, the schematic of the relation between the light polarization angle and molecular orientation is illustrated. This means that by tracing the intensity variation as a function of changing the angle, one should be able to determine the orientation of the adsorbed molecules on the substrate.
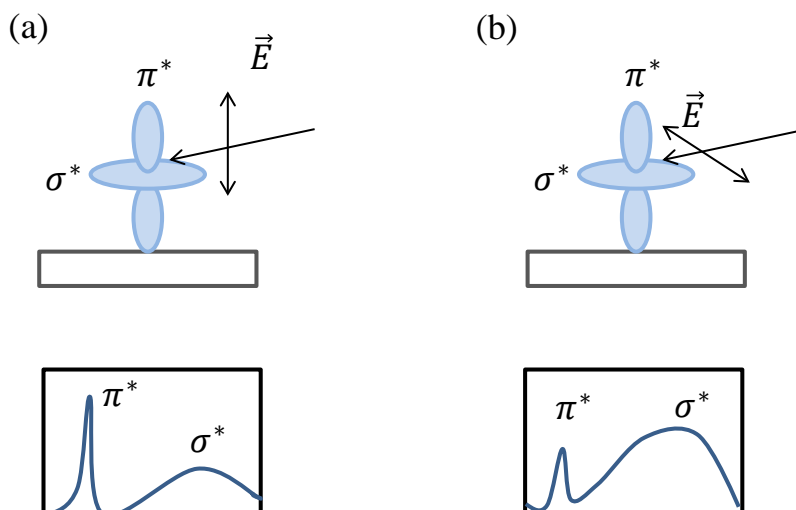
Figure 2-9: The schematics illustrate the polarization dependence of NEXAFS for π^* and σ^* orbitals under **(a)** p-polarization and **(b)** s-polarization.

In the work presented in this thesis, the light is linearly polarized. Experimentally we have changed the incident angle and recorded different XA spectra. An example of XA spectrum is presented in Figure 2-8. X-ray absorption spectra from a monolayer and a thick film of ZnPc on Pt(111) were measured in 3 different angles. The NEXAFS measurement angles are: θ: 0°, 40° and 80° (θ: The angle between E vector and surface plane). Knowing the orbital configuration in phthalocyanines (π orbitals normal to the molecular plane and σ orbitals in the molecular plane), this multi-plot demonstrates that the molecules are lying almost parallel to Pt(111) in the monolayer (ML), while they are tilted in the thick film ($\varphi < 45°$, φ: the angle between the molecular plane and the substrate).

2.3: Scanning Tunneling Microscopy

Scanning tunneling microscopy (STM) is a microscopy method which allows imaging the real space with atomic resolution. STM was developed at 1981 by Binning and Heinrich Rohrer, and was awarded the Nobel Prize in Physics in 1986[52–54]. This technique is based on the quantum tunneling effect, which allows the electron to tunnel through a potential barrier between two conductors provided that the gap is small enough (couple of Ångströms). This gap can be vacuum or even air or liquid, where the energy of the potential barrier is larger than the energy of tunneling electron. Tunneling effect is the result of overlap between the wave function of two conductive surfaces, i.e. the transition takes place via this wave function overlap despite the gap of a few Ångströms. In this case,

electrons can tunnel in both directions, from one conductor to another, causing a zero net current. In order to achieve a net current, a bias is applied between the two conductors.

In an experimental STM set up, a very sharp (ideally monoatomically sharp) conductive tip (commonly made of W or Pt-Ir) scans over a relatively flat surface. The surface has to be metal or semiconductor for the tunneling effect to happen. Since the distance between the tip and the sample should be kept very small (couple of Å), roughness of the sample should not be too high, which would result in either disturbing the tunneling during the measurement or crashing the scanning tip. Therefore, this measurement requires samples of high quality and careful surface –science sample preparations.

As mentioned earlier, in order to control the direction of electron tunneling, a voltage should be applied between the conductive surfaces. So we need to add a small bias between the tip and the conductive sample. Depending on the polarity of the applied voltage, electrons can tunnel to or from the tip. Schematic illustration of energy levels corresponding to the sample and the tip is presented in Figure 2-10.
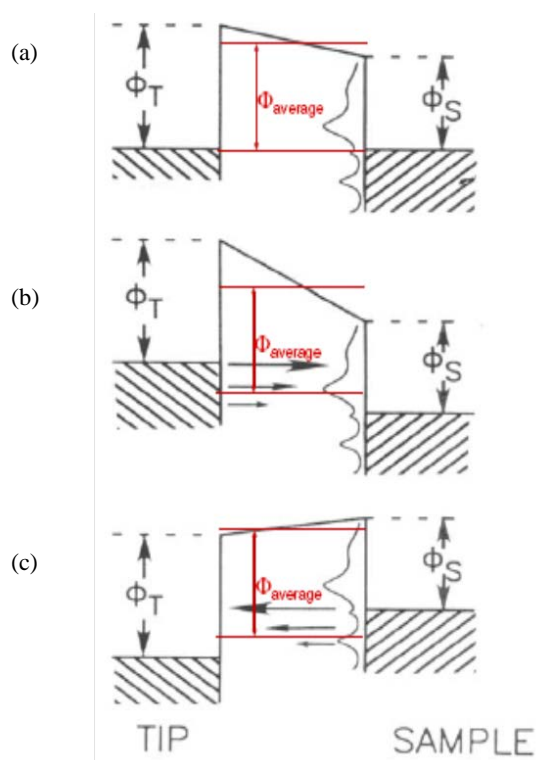
Figure 2-10: A schematic representation of the principle of STM, for **(a)** zero bias voltage, **(b)** positive bias voltage and **(c)** negative bias voltage. (Figure taken from[55])

As shown in Figure 2-10, if a negative bias is applied to the sample, the electron flow is from the sample to the tip. These electrons are from the occupied states of the sample which will tunnel to the tip, giving information about occupied states of the sample. On the other hand, applying a positive bias to the sample changes the electron flow; from the tip to the sample. These electrons will tunnel to the unoccupied states of the sample (unoccupied molecular states or conduction band states), carrying information of the unoccupied electronic states of the sample.

As explained above, the basic principle of STM is the quantum tunneling effect, in which the tunneling current has an exponential relation with the distance between the two conductors. (See equation 2.3). This correspondence enables this technique to map the topography as well as the electronic structure of the studied sample's surface by simply scanning over it.

$$I \propto \exp\left(-2d\,\frac{\sqrt{2m(\Phi_{average}-E)}}{\hbar}\right) (2.3)$$

In Figure 2-11, schematic view of STM setup is demonstrated. The function of STM can simply be described as following. A coarse motion moves the tip towards the surface until the distance is small enough for tunneling to take place. This is controlled by the applied voltage and the reference tunneling current. From this position, the tip's motion is controlled by piezo components, usually X, Y and Z components. X and Y are used to scan the tip over the sample and the Z component is responsible for adjusting the tip-surface distance. The tip's Z control is done in different ways, determined by the imaging mode.
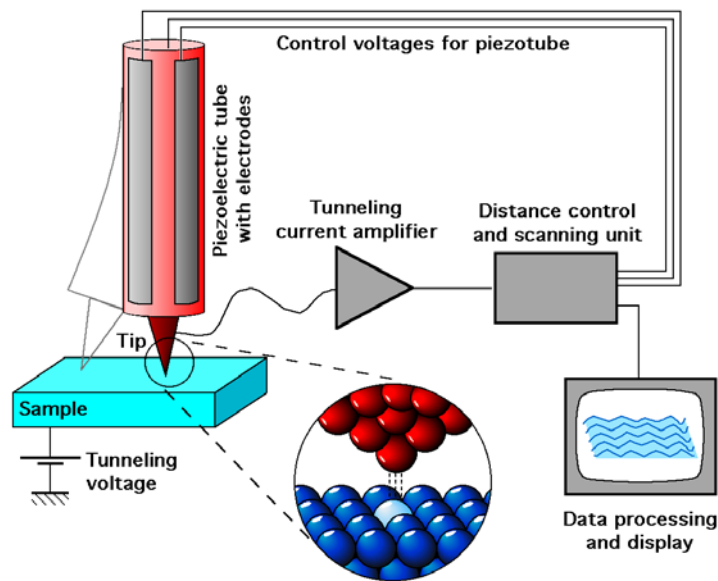
Figure 2-11: Schematic of STM (Courtesy to Michael Schmid, TU Wien)

Imaging with STM can be carried out, using two different methods. These imaging modes are known as constant-current and constant-height modes. In constant-current mode, the tunneling current signal which is transferred to the control unit will be compared to the set-point in the feedback loop. Then, the control unit sends a signal to the Z component to change the height until the tunneling current matches the set-point. Variations in the tip position provide a topographical map of the surface, which will be recorded as an STM image. The other imaging mode is the constant-height mode, in which the tip-surface distance is kept fixed and the feedback loop is not active. Variations of tip position, which keep its distance constant from the surface, correspond to the topography of the surface and cause

fluctuations in the tunneling current. These current changes will be translated to topography in the calibrated control unit. The drawback of the constant-height mode is that the feedback loop, which can control the tip-surface distance and prevent the tip from crashing is deactivated. Hence the constant current mode is the most common imaging mode in tunneling microscopy.

The extremely small tip-surface distance together with the highly precise piezo movement, results in very high resolution obtained in this microscopy technique (0.01 Å, vertical resolution and about 2 Å, lateral resolution), which makes it a highly local tool to probe the electronic properties of surfaces. Giving an atomically resolved image of surfaces and adsorbate layers, STM provides the opportunity to investigate the atomic arrangements at the surface and possible surface reconstructions.

The STM images presented in this thesis are obtained via two different microscopes; Omicron VT-STM and RHK (UHV SPM 3500). In both cases, measurements are performed in UHV and in-situ sample preparations are carried out. Image processing is done using WxSM. (more details on preparation methods are mentioned in the articles.)

2.4: Low Energy Electron Diffraction

Low energy electron diffraction is a technique employing elastic scattering of electrons from the surface to reveal information about the surface reconstructions. Importance of the investigation on atomic orders at the surface comes from the fact that sometimes atoms arrange themselves differently at the surface of a material with respect to the bulk, causing changes in the unit cell parameter. These new arrangements as result of relaxation or reconstruction take place to reduce the total energy.

Elastic scattering or diffraction of electrons is a standard technique to obtain structural information of surfaces[56]. The basic diffraction condition in LEED can be described the same as in x-ray diffraction. The scattering parameter should satisfy Bragg's law (equation 2.4).

$$n\lambda = 2d\,\sin\theta \ (2.4)$$

("n": an integer, λ: the wavelength of incident wave, d: the spacing between the planes in the atomic lattice and θ: the angle between the incident ray and the scattering planes.)

Results of a LEED measurement contain information of the unit cell parameter as well as the location of atoms in this unit cell. Information of the former (lattice parameter) is extracted by a reverse transformation, since the diffraction pattern corresponds to reciprocal lattice. However determination of the coordination of atoms requires detailed studies, which is not included in the scope of this work.

The experimental setup for LEED comprises of the following parts; an electron gun to produce the electron beam and a display system to show the Bragg diffraction spots. A typical four-grid LEED system is shown in Figure 2-12.
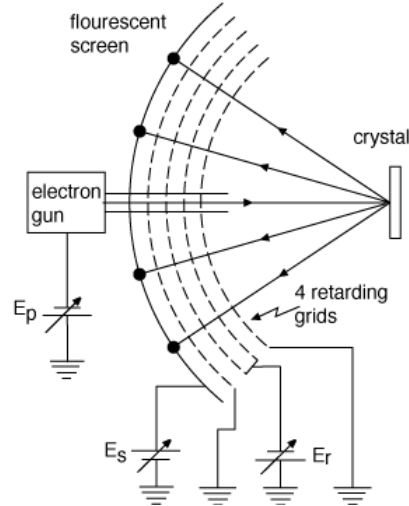
Figure 2-12: The schematic of a four-grid LEED optics.

The electron gun is located in the center of the diffractometer. The electron gun produces an electron beam with the beam diameter of about 1mm or less and the energy range ~ 10-500 eV. The LEED experiment is based on the electron acceleration from the electron gun. Acceleration occurs by applying a variable voltage which affects the kinetic energy of the emitted electrons. Once the electrons hit the sample, they will be diffracted and pass through vacuum toward a series of grids. To get a field-free region, the first grid is grounded; in second and third ones variable voltage (the suppress voltage) is applied to filter out the inelastically scattered electrons. A high voltage is applied between fourth grid and the screen which gives the electrons enough energy to light up the phosphor screen and reveal the diffraction pattern.

 The electron wavelength is given by de Broglie equation 2.5.

$$\lambda = \frac{h}{\sqrt{2mE}} \ (2.5)$$

In this equation, *h* is Planck's constant, *m* is the electron mass and *E*, the energy of electrons.

Since the interatomic distances in solids are a few Å, the electron wavelengths are selected in this range, meaning the acceleration energy of the electrons in the electron beam is about 30 to 500 volts. Recording and analysis of the diffraction pattern reveals the arrangement of the atoms on the surface. Also sharpness of the pattern describes the extent of order of atoms on the surface.

In Figure 2-13(a), an example of a LEED pattern is demonstrated, in which the Au(111)-I $(5 \times \sqrt{3})$ reconstruction is depicted. Figure 2-13(b), shows a calculated pattern of the same reconstruction.

5x√3
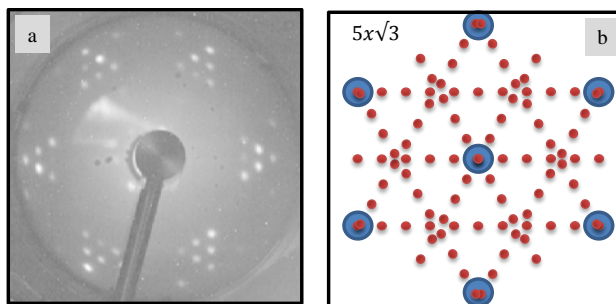
Figure 2-13: (a) and (b) are the measured and calculated LEED pattern of the Au(111)-I(5 × √3) surface reconstruction.

Chapter 3

Adsorbates and Substrates

3.1: Adsorbates

3.1.1. Metal-Phthalocyanines (MPcs)

Phthalocyanines are synthetic macro cyclic compounds, constructed of four lobes; each lobe is composed of one pyrrole and one benzene group. Metal-free phthalocyanine (H_2Pc) is noted as $H_2C_{32}N_8H_{16}$ (Figure 3-1(a)). The flexibility of this molecule provides an opportunity to replace the two central H atoms with a metallic atom (MPc) (a metal-oxygen or metal-halogen can also be inserted to Pc center). Depending on what would occupy the center, the molecule can possess a planar or a non-planar configuration. In most cases the molecule remains planar except when a big metallic atom e.g, Sn or Pb occupies the center. Moreover, if a polar component such as TiO replaces the two H atoms in the center, the molecule will possess a shuttle-shaped geometry.
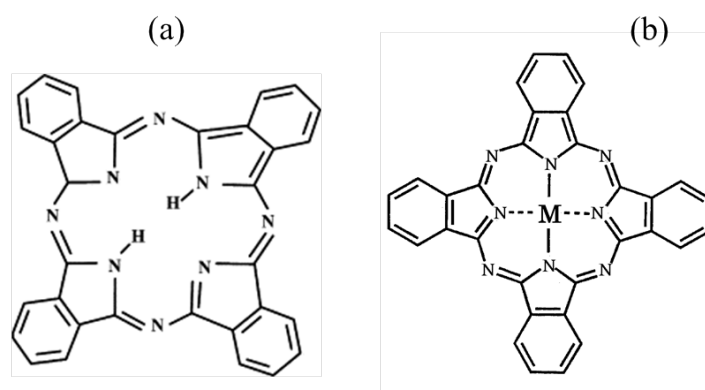
Metal-free Phthalocyanine   Metal Phthalocyanine

Figure 3-1: Molecular structure of **(a)** metal-free phthalocyanine and **(b)** metal phthalocyanine.

The various features, such as electronic, optical and magnetic properties of Pcs can be tuned by changing the metallic center[57–61]. In particular, transition metal phthalocyanines has gained lots of attention, owing to the significant effect of d-orbitals on properties of the molecules[21–23,62–72].

These molecules can create self-assembled layers, making the thin film processing very convenient[23,57,58,62,73–76]. These intrinsically semiconducting molecules, show a very high thermal (stable up to 500℃) and chemical stability in addition to their electronic, optical and magnetic properties. These characteristics make MPc a promising candidate to be used in organic solar cells, organic light-emitting diodes (OLEDs) and organic field-effect transistors (OFETs). The function of these devices is influenced by another essential factor; the interaction and charge transfer at the interface of MPc layers and the substrate. Charge transfer at the interface of MPc and the substrate can determine the layer growth mode, molecular configuration, magnetic and electric properties of the molecular layer, which would effectively modify the organic-device functions. More manipulation of MPc-substrate interaction is possible by either decorating the molecules (adding external atoms or molecules to the center or periphery of Pcs)[35–37] or modifying the substrate by inserting an intermediate layer[38,39]. Adding a layer on top of MPc-substrate has been also reported[40–44].

In this thesis MgPc, FePc and ZnPc are studied. In MgPc and ZnPc, HOMO (Highest Occupied Molecular Orbital) and LUMO (Lowest Unoccupied Molecular Orbital) have only contributions from organic ligand, while HOMO and LUMO of FePc have considerable contributions from Fe d orbitals. This is described by d orbital of Fe being open-shell type while Zn has a closed d-shell. Zn^{2+} and Mg^{2+} show a similar electronic configuration having fully filled sub-shells. However adsorption of these molecules on different substrates results in change in the orbital configuration and the participation of each orbital in interfacial interactions.

3.1.2. 4-tert-butyl pyridine (4TBP)

4tert-butylpyridine is a heterocyclic molecule which possesses the structure of a pyridine, in which one of the hydrogen atoms (position 4) is replaced by a tert-butyl $[-C(CH_3)_3]$ group. The schematic illustration of chemical formula of both pyridine and 4tert-butyl pyridine (4TBP) is presented in Figure 3-2. Pyridine itself is actually made of a benzene ring which has accommodated a nitrogen atom by replacing a methine-group $(C-H)$ with the chemical formula of C_5H_5N. Pyridine is a colorless liquid which is soluble in water. It is a weakly alkaline, highly flammable compound with unpleasant fish-like smell. 4TBP is known to be a significant additive to the electrolyte of DSSCs. There have been several works which have investigated the effect of 4TBP on the function of DSSCs. Following results have been reported.
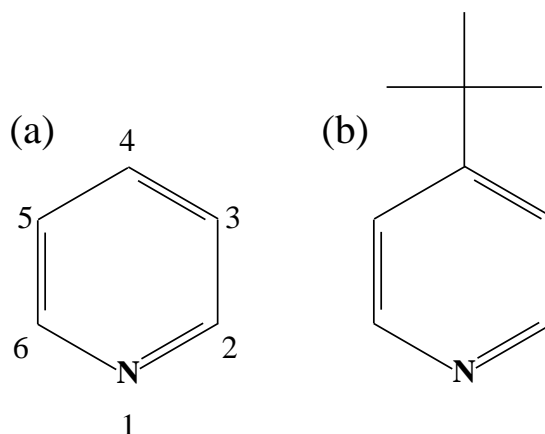
Figure 3-2: Chemical formula of (a) pyridine and (b) 4.tert-butyl pyridine (4TBP).

Upon addition of 4TBP to the (I_3^-/I^-) electrolyte, the fill factor and open circuit voltage are increased without affecting the short circuit current[46]. These effects are described by occupying active sites of TiO_2 by 4TBP[77].

In different studies, a 4TBP-induced shift of the conduction band edge of TiO_2 to lower binding energies was found to be responsible for enhancement of open circuit voltage. Moreover, 4TBP reduces the concentration of protons and other cations in the electrolyte and remove them from the substrate. These cations are known to induce band bending in TiO_2 conduction band edge in the opposite way as 4TBP. Besides, 4TBP blocks the transport of tri-iodide to the surface and removes adsorbed iodine from the surface reducing the electron recombination from TiO_2 to tri-iodide in the electrolyte[78,79].

3.2: Substrates

3.2.1. Au(111) and iodated surfaces

Au(111)

The clean Au(111) surface has a ($22 \times \sqrt{3}$) reconstruction[80], also known as the herringbone structure. This surface is the only (111) surface between closed-pack fcc metals, which is reconstructed. In Figure 3-3, two STM images from the clean surface are presented. Figure 3-3(a) shows large flat terraces separated by monoatomic steps (1.3Å) and Figure 3-3(b) illustrates the herringbone structure. The herringbone structure consists of dark (lower) and bright (higher) regions. The surface plane of Au(111) has more atoms than the bulk plane (4% higher). The surface is described by a stacking-fault-domain model. In this surface, different areas (fcc and hcp) are periodically stacked. These two regions are separated by a domain wall (also known as soliton wall) from each other.

As Figure 3.3(b) shows, fcc and hcp areas appear darker in the STM image than the domain walls. It means that these regions (hcp and fcc) are located lower than domain walls, which appear as brighter stripes between the two hollow site regions. A closer look in the image reveals that the widths of the dark regions are different; wider regions have fcc and narrower ones have hcp stacking[26].
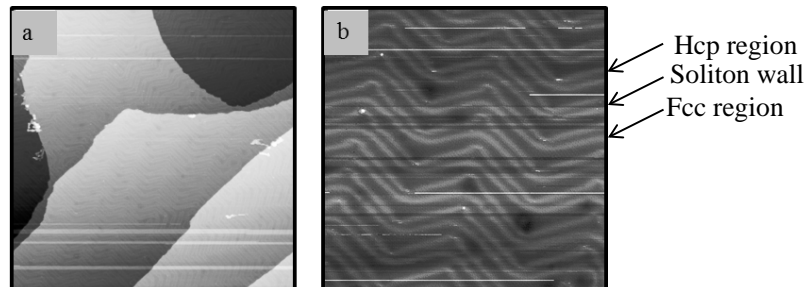
Figure 3-3: STM images of Au (111) surface; **(a)** 300x300 nm^2 showing large flat terraces separated by monoatomic steps (1.3 Å) and (b) 70x70 nm^2 herringbone structure is visible. Fcc and hcp regions and soliton wall are marked panel **(b)**.

Au(111)-I$(\sqrt{3} \times \sqrt{3})$R30°

After iodine deposition, the herringbone structure disappears. One of the possible Au(111)-I structures is the $(\sqrt{3} \times \sqrt{3})$R30°, which is a common organization found after deposition of smaller adsorbates on the (111) surface of transition metals[81–83]. This structure most often holds 1/3 monolayer (ML) of adatoms (1 ML corresponds to the number of gold atoms on the bulk terminated 111-surface). STM image and LEED pattern of this surface, together with the atomic model are presented in Figure 3-4.
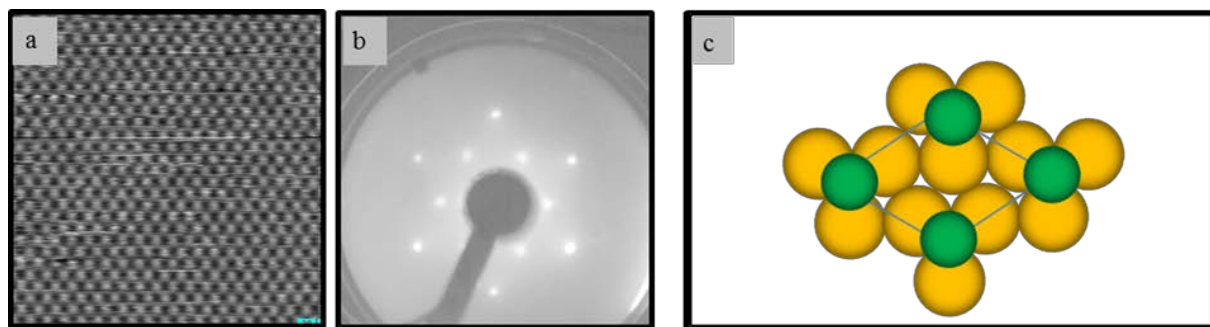
Figure 3-4: (a), (b) and **(c)** are STM image (+0.38 V, 0.7 nA), LEED pattern and atomic model of the Au(111)-I$\left(\sqrt{3} \times \sqrt{3}\right)R30°$ surface. The unit cell is outlined in the model.

In the present case, it was suggested based on IV-LEED that every iodine atom is in contact with three gold atoms in the hcp-hollow sites[84]. Our calculations give a slight preference for the fcc site as some other theoretical studies of the halogen adsorption on transition metal surfaces did, however the energy difference between the two sites is very small[85,86]. STM and LEED (as used here) are not able

to tell the difference between these two sites, therefore an atomic model of this reconstruction in Figure 3-4(c) is presented with iodine atoms in (unspecified) hollow sites.

Au(111)-I ($5 \times \sqrt{3}$)

At the saturation limit for our deposition method, a ($5 \times \sqrt{3}$) structure was achieved. Higher coverage structures are only observed with an over-pressure of iodine[83] or in electrochemical conditions. The STM image in Figure 3-5(a) displays the surface with atomic resolution, which fits nicely with the atomic positions in the structure model on the right hand side (Figure 3-5). This structure has been observed by STM[81,87] and LEED[88] as discussed previously, and is known to appear in the coverage range $0.33 < \theta < 0.4$. Surface X-ray Scattering (SXS) measurements in electrochemical conditions have also reported (p$\times \sqrt{3}$) structures with p varying with the applied electrochemical potential, suggesting an uni-axial compression of the ($\sqrt{3} \times \sqrt{3}$)R30° structure to form a striped phase[82].
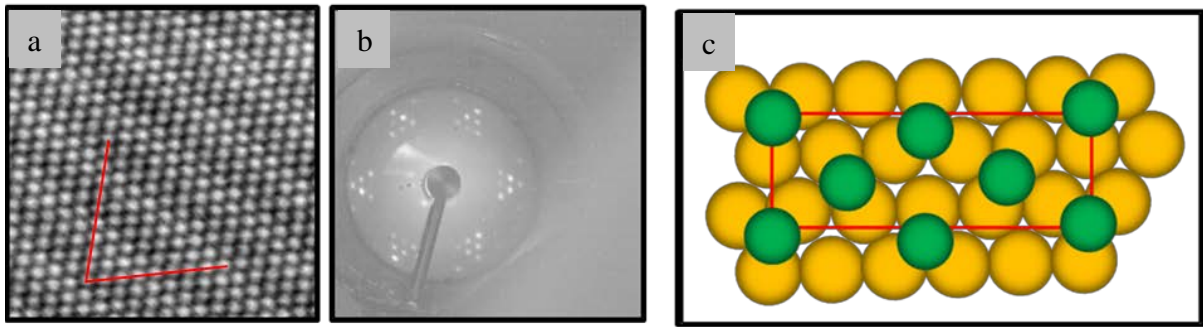
Figure 3-5: (a), (b) and **c** are STM image (-0.27 V, 8.1 nA), LEED pattern and atomic model of the Au(111)I-(5×√3) structure. The unit cell is outlined in the model.

Basically by compressing the ($\sqrt{3} \times \sqrt{3}$) structure perpendicular to one of the $\sqrt{3}$ directions, a higher coverage of iodine can be accommodated on the substrate, which eventually will lead to a ($5 \times \sqrt{3}$) LEED pattern[88]. The compression inevitably forces some iodine away from their hollow (hcp) sites into bridge and the other hollow (fcc)[88]. Thus, whether iodine sits in the fcc or hcp hollow on the ($\sqrt{3} \times \sqrt{3}$) structure does not affect the positions in the ($5 \times \sqrt{3}$) reconstruction.

3.2.2. Pt(111) and iodated surface

Pt(111)

As mentioned in section 3.2.1, fcc(111) closed-packed surfaces excluding Au, do not reconstruct. For an ideally terminated Pt(111), the top interlayer spacing is prominently expanded by 0.025 ± 0.01 Å (1.1%). Charge reorganization at the surface induces strengthening of intralayer bonding in expense of interlayer bonding, causing the expansion of the first metal layer spacing[89].

Pt(111)I-$(\sqrt{3} \times \sqrt{3})R30°$

At 1/3 ML iodine coverage on Pt(111) is reconstructed to a $(\sqrt{3} \times \sqrt{3})R30°$. At this layer iodine atoms only sit on 3-fold sites which provide stronger Pt-I bonding. The $(\sqrt{3} \times \sqrt{3})$ model is given in Figure 3-4, the same as for Au(111)-I $(\sqrt{3} \times \sqrt{3})$.

Pt(111)I-$(\sqrt{7} \times \sqrt{7})R19°$

Further adsorption of iodine on Pt, creates a saturated layer with a $(\sqrt{7} \times \sqrt{7})R19°$ reconstruction (see Figure 3.6).
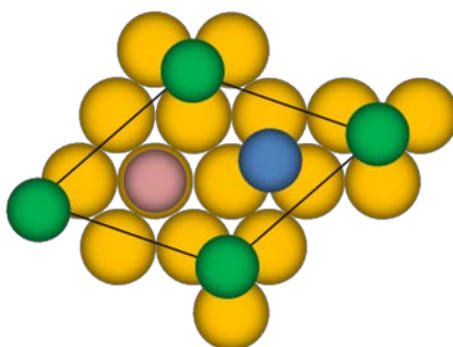
Figure 3-6: atomic model of the Pt(111)-I $(\sqrt{7} \times \sqrt{7})R19°$ structure.

This reconstruction is confirmed by our LEED investigations. In this layer iodine atoms occupy three different sites, 3-fold sites (hcp and fcc) and atop sites[90]. (The 3-fold sites are not equivalent, there are two different 3-fold sites; one with a Pt atom directly under and the other one without. The ones with a Pt atom directly under are more favored for electronegative adatom (iodine in this case)). Photoelectron spectroscopy results from I4d enable us to distinguish the iodine atoms in 3-fold and 1-fold (atop) sites (discussed in paper III).

3.2.3. TiO$_2$(110)

Rutile TiO$_2$

There are three diverse crystallographic modifications of titanium dioxide called rutile, anatase, and brookite. Rutile is the most common one in research due its various technological applications such as, photo assisted heterogeneous catalysis, energy conversion, gas sensors and protection layers. In this thesis only single crystalline rutile has been used.

In the rutile bulk structure Ti^{4+} ions are six fold coordinated while O^{2-} is three fold coordinated. There are two formula units in each unit cell. Having a relatively wide band gap, 3.1 eV, rutile TiO$_2$ is often considered an insulator in which the valence band is mostly made of O2p orbitals and the conduction band is mostly Ti3d derived[91,92].

Pure TiO$_2$ crystals are transparent. However, intrinsic defects (like oxygen vacancies or Ti interstitials) affect the conductivity and optical properties of the crystal. For example, the transparent crystal becomes light or dark blue, depending on the amount of defects. The transformation is consequence of sample reduction, which can be carried out simply by heating the sample (up to ~1000 K for a few hours) in UHV. This is done on purpose in the initial steps of sample preparation to enhance the conductivity of the sample. Upon this heat treatment, sample changes to an n-type semiconductor which allows STM measurements. Besides, the charging problem during XPS and LEED measurements will be avoided by reduction of TiO$_2$.

The (110) surface

The (110) surface is the most stable surface in the rutile crystal structure, with the lowest surface energy and because of that they are formed in microscopic crystals. The schematic of the rutile (110) surface is given in Figure 3-7.
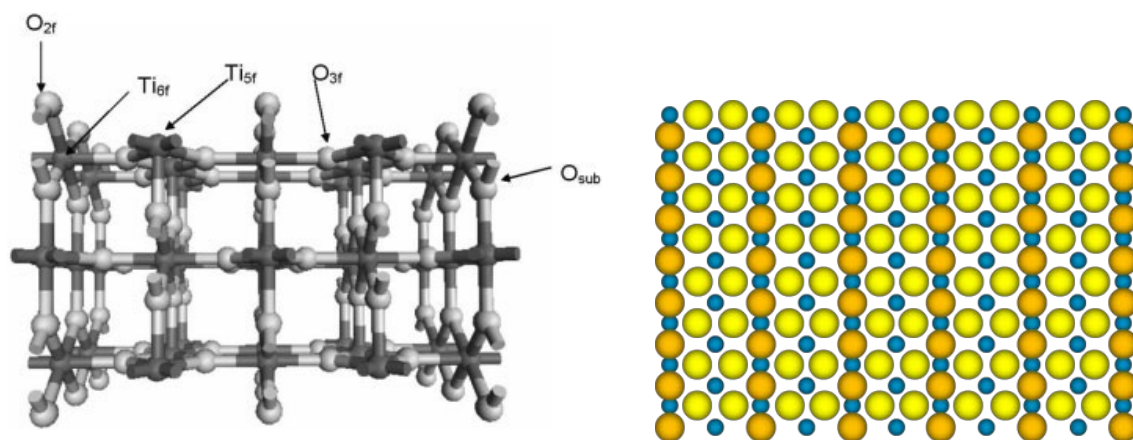

Figure 3-7: Schematic figure of the rutile (110) surface, and a top view of the (1x1) surface.

Through formation of a surface, bonds are broken, which generates atoms with different co-ordination than in the bulk. Titanium ions are 6-fold coordinated in the bulk. At the surface there are two different types; 6 fold coordinated, Ti_{6f}, and 5-fold coordinated, Ti_{5f}. There are also different oxygen ions; O_{sub} are 3-coordinated oxygen ions in the bulk. O_{3f}, are 3-fold coordinated oxygen ions at the surface. In addition there is also 2-fold coordinated (bridging) oxygen, O_{2f}, which binds to two Ti_{6f}. So the surface has rows of Ti-ions and rows of bridging oxygen.

In STM images from this surface one can see dark and bright rows, which correspond to Ti and O rows. The brighter rows are Ti and the darker run along the oxygen rows. The rows are separated by ~ 6.5 Å. In addition there are numerous bright spots in the oxygen rows. They are due to oxygen vacancies, formed by removal of bridging oxygen. The amount of oxygen vacancies depends on the sample history, time and temperature of heating. By creation of the bridging oxygen vacancy, two associated electrons will be left behind and they result in formation of Ti^{3+} ions. The STM image was achieved by applying a negative bias, i.e, tunneling from occupied states of TiO_2. The oxygen vacancies are electron rich and therefore appear brighter in the image. Oxygen vacancies at the surface act as dopants and play a crucial role for the reactivity.
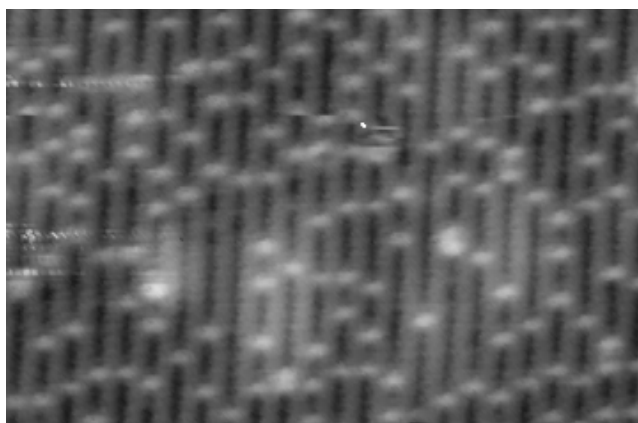
Figure 3-8: Filled state STM image from the $TiO_2(110)$ surface with plenty of oxygen vacancies (bright spots).

The effect of surface oxygen vacancies is perhaps most visible in valence band spectra. In Figure 3-9 two photoemission spectra from $TiO_2(110)$ at low binding energy are shown[93]. The two vertical lines in the figure indicate the valence band edge and the Fermi level, respectively. The top spectrum is from the clean (1×1) surface with a strong state in the bulk band gap. The origin is the oxygen vacancies on the surface. By adsorption of 4TBP, lower spectrum, the intensity is reduced. Depending on the sample history etc, it is not always possible to remove this state. It has other contributions than surface oxygen vacancies.
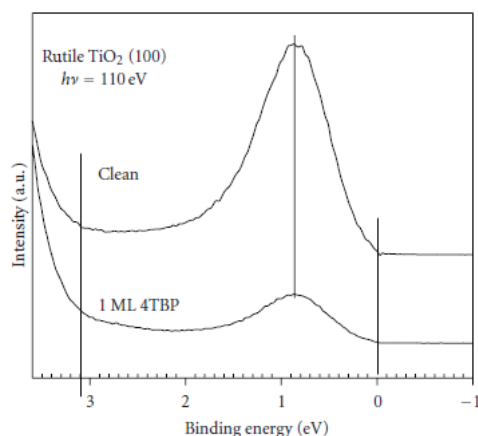
Figure 3-9: Photoemission spectra from TiO$_2$(110) before and after adsorption of 4TBP. The peak at 0.9 eV is due electrons in oxygen vacancies. Their intensity is reduced after 4TBP adsorption.

By elevating the time or temperature of heat treatment, the reduction is enhanced, which results in dark blue sample, possessing a (1×2) reconstruction. An atomic model of the (1×2) reconstruction is shown in figure 3-10. Large balls are oxygen and small balls are titanium. The rows of red O and black Ti together with the atoms just below form Ti$_2$O$_3$ like added rows on the surface. Further heat treatment leads to the so called (1×2) -cross linked (CL) surface. It is very similar to the (1×2) except that the added rows are broken and partly shifted.
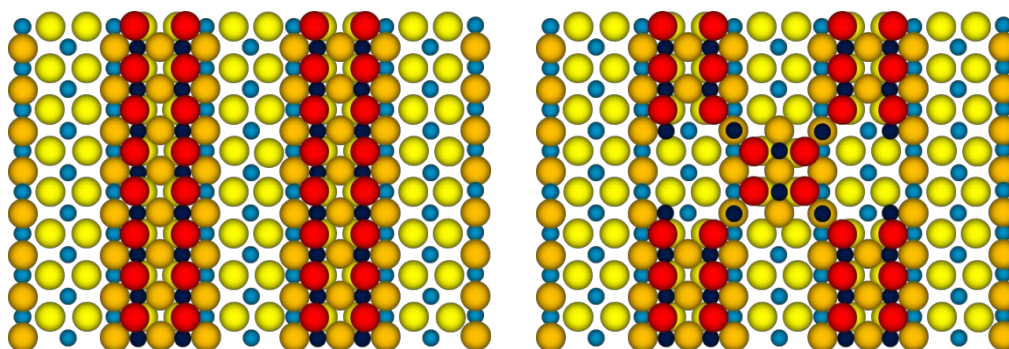
Figure 3-10: Atomic model of the TiO$_2$(110) $(\mathbf{1 \times 2})$ and TiO$_2$(110) $(\mathbf{1 \times 2})$-CL surface structures.

Chapter 4

Results and discussion

4.1: ZnPc and FePc on Au(111) and Au(111)-I surfaces

Adsorption of Zinc phthalocyanine (ZnPc) and iron phthalocyanine (FePc) thick films and monolayers on Au(111) and AuI surfaces are studied, using photoelectron spectroscopy and X-ray absorption spectroscopy(Paper I and II)[23]. Both molecules adsorb flat on Au(111) at monolayer. Work function changes indicate that both molecules donate charge to Au, through the π-system. The work function is a sensitive measure of changes on the surface; charge transfer between adsorbate and substrate, interface dipoles and adsorbate dipoles may all contribute to the changes of work function. In PES the low-energy cut-off determines the work function. After molecular deposition, the cutoff shifts to lower kinetic energy as listed in Table 4.1.1, which translates to a reduced work function according to $\Delta\Phi = \Phi_{Pc} - \Phi_{Au}$[94], by about 0.3-0.8 eV, which is within the range typically observed in literature[95]. This shift is caused by formation of an interface dipole, and the direction of the shift is traditionally interpreted in terms of an electron transfer from the organic layer to the metal substrate[96,97].

In order to obtain a clearer image of the energy level alignment at the interface of Au and Pc, the hole injection barrier (Δ_h) is also investigated, which is achieved by measuring the distance between the HOMO edge (linear extrapolation of the low binding energy onset) and the Fermi level. The schematic energy level alignments are presented in Figure 4-1.1.

a) ZnPc/Au,ML

$E_{vac(Au)}$

$\Delta\Phi$:-0.3eV

$E_{vac(FePc)}$

Φ:5.48eV

E_{Fermi}

Δ_h:0.42eV

Au(111)   **ZnPc**

c) FePc/Au,ML

$E_{vac(Au)}$

$\Delta\Phi$:-0.31eV

$E_{vac(FePc)}$

Φ:5.48eV

E_{Fermi}

Δ_h:0.48eV

Au(111)   **FePc**

b) ZnPc/Au,TF

$E_{vac(Au)}$

$\Delta\Phi$:-0.68eV

$E_{vac(FePc)}$

Φ:5.48eV

E_{Fermi}

Δ_h:0.7eV

Au(111)   **ZnPc**

d) FePc/Au,TF

$E_{vac(Au)}$

Φ:5.48eV

E_{Fermi}

Δ_h:0.7eV

Au(111)   **FePc**
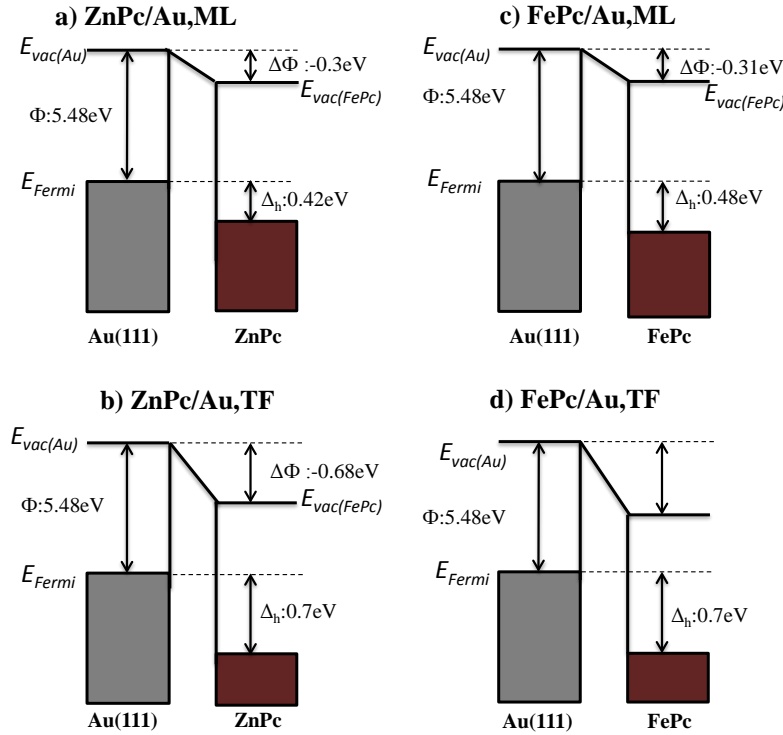
Figure 4-1.1: Schematic energy level diagrams; a) monolayer, b) thick film of ZnPc/Au(111), and c) monolayer and d) thick film of FePc/Au

Table 4.1.1. Work function changes and hole injection barriers from the clean Au(111) surface and after various preparations with ZnPc and FePc.

	Φ(eV)	$\Delta\Phi$ (eV)	Δ_h
Au(111)	5.48		
FePc, ML	5.17	-0.31	0.48
FePc, TF	4.66	-0.82	0.7
ZnPc, TF	4.8	-0.68	0.7

4.1.1. Monolayer versus thick film

As mentioned above, both ZnPc and FePc are adsorbed parallel to Au(111) in the monolayer region. ZnPc keeps this orientation in all investigated coverages, whereas FePc molecules stand up in the thick film. The stronger intermolecular interaction between FePc molecules leads to change of orientation, as well as higher conductivity in FePc layer in comparison with ZnPc, which is reflected in thickness-dependent differences of core-level shifts. This is due to differences in molecular orbitals of ZnPc and FePc, which will be further discussed in 4.1.2.

The binding energy of C1s and N1s core-level spectra measured from ZnPc and FePc layers on Au(111) are listed in Table 4.1.2. This shows that thickness-dependent shifts are bigger for carbon atoms than nitrogen atoms. Besides, ZnPc spectra possess larger thickness-dependent shifts compared to FePc spectra. This is a typical behavior for organic thin films; the thicker films tend to shift to higher binding energy, often explained as a reduced screening of the core hole[28]. Nevertheless, the FePc thick film is slightly thicker than the one of ZnPc, it experiences a smaller coverage-dependent shift. Thus there should be another origin for the observed difference. One possibility is the difference in ordering and orientation of the two films, which would lead to different conductivity and screening. Furthermore, the ZnPc spectrum is broader than the FePc spectrum, also indicative of a better conductivity and screening by mobile carriers in FePc. When charge carrier screening is poorer, polarization screening will become more important which excites more vibrations.
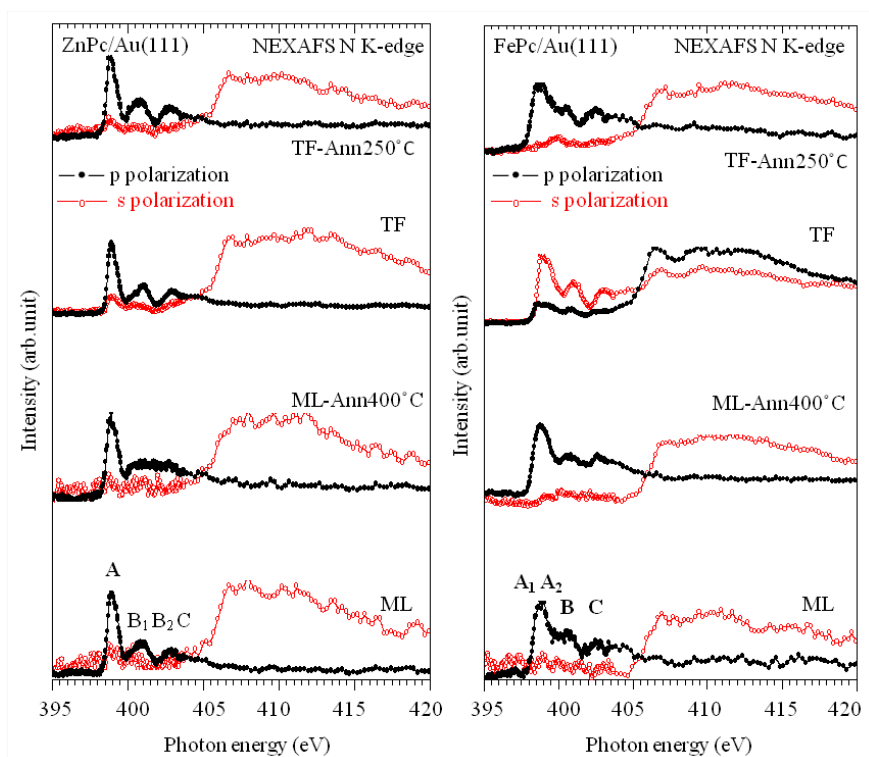

Figure 4-**1.2:** N K-edge NEXAFS spectra at different preparations under p and s polarization for (a) ZnPc and (b) FePc molecules on Au(111)

Table 4.1.2. Binding energies (in eV) for C1s and N1s at different preparations. The values refer to the experimental peak positions.

	ML	Thick	ΔE
FePc-C_B	283.85	284.25	0.40
FePc -C_P	285.16	285.54	0.38
FePc -N	398.29	398.49	0.20
ZnPc-C_B	283.61	284.58	0.97
ZnPc -C_P	284.99	285.98	0.99
ZnPc -N	397.91	398.61	0.70

In Figure 4-1.3, near-Fermi region of valence band spectra for ZnPc and FePc layers on Au(111) are presented. ML of ZnPc, shows an interface HOMO at 0.7 eV below Fermi level. By increasing the thickness, HOMO shifts to higher BE and fully develops to the molecular HOMO of the thick film at 1.35 eV. The thickness dependence of the FePc VB is similar to that of ZnPc: the interface-HOMO appears at 0.72 eV at ML coverage and develops to a molecular HOMO at 1.50 eV by increasing the layer thickness. However there is an additional feature in the FePc monolayer spectra at 0.13 eV (I_0) which does not exist for ZnPc spectra and will be discussed in 4.1.2.
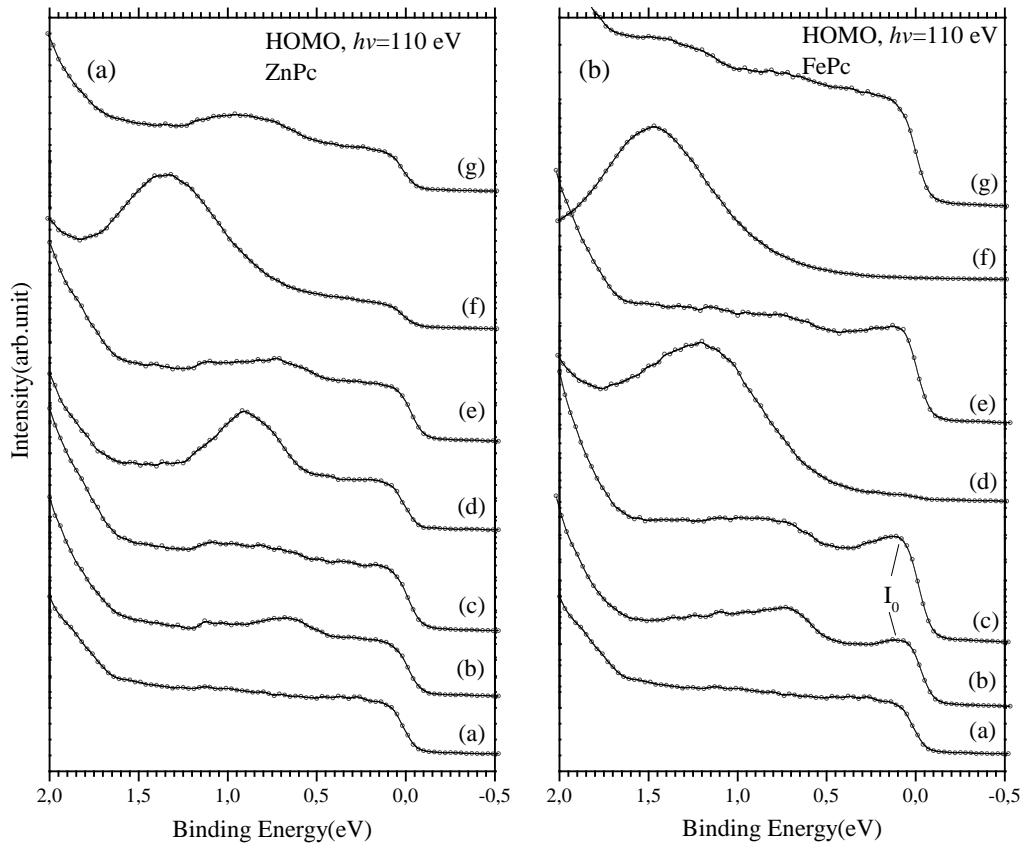
Figure 4-**1.3:** HOMO region near the Fermi level for ZnPc in panel **(a)** and FePc in panel **(b)**. The letters (a) to (g) in the figure refer to the sample preparations. a) clean Au, b)1ML ZnPc, c) b annealed at 400- °C, d) a few ML, e) d after annealing, f) thick (bulk-like) film, g) f after annealing.

4.1.2: d-orbital occupancy

As mentioned above, significant differences were observed between FePc and ZnPc adsorbed on Au(111); there is an additional feature in the HOMO region of the FePc monolayer spectrum at 0.13 eV (I_0) which does not exist for ZnPc (Figure 4-1.3). This peak shows the highest intensity at ML coverage (graph c, Figure 4.1.3) and decreases at higher coverage and disappears from the thick film spectrum. A similar state was observed by Gargiani *et al*. for FePc on Au(110)[72]. This peak was explained as states residing on the central metal atoms, possibly involved in the interaction with Au. Inverse photoemission identified the LUMO close to the Fermi level for both FePc and CoPc. Therefore, the I_0 peak in FePc ML spectra, very close to the Fermi level was said to be due to charge transfer from the metal states to the former LUMO.

The valence electronic structure of FePc shows a considerable difference from ZnPc; the HOMO and HOMO-1 (very close in BE) are C2p-Fe 3d-like in FePc, while HOMO in ZnPc is located on the phthalocyanine ring. Fewer electrons in the d band of Fe atom compared to Zn, let the metal d orbitals take direct part in the interaction with the substrate, which enhances the interaction states close to the Fermi level. As mentioned above, this state is caused by charge transfer from the metal states to the former LUMO [72]. This is in excellent agreement with previous STM studies, where it was shown that for FePc and CoPc on Au(111), Fe (d^6) and Co (d^7) atoms appear higher in the molecular images, 0.25 nm and 0.3 nm respectively. On the other hand, in NiPc (d^8) and CuPc (d^9) images the central metal atom appears as a hole (measured with ±0.5 V biased sample for FePc and NiPc, and -0.1 to 0.9 eV in CoPc and CuPc)[98,99]. The interpretation points out that LUMO in Fe(II)d^6 and Co(II)d^7 are of significant d-orbital character near the Fermi energy, while it is not the case for Ni and Cu. It seems reasonable to use the same argument for ZnPc. In ZnPc, the filled d-orbital, Zn (d^{10}) does not contribute to the interaction with the substrate as much as Fe (d^6) does, which explains the absence of the peak just below the Fermi level in ZnPc valence spectra.

Knowing the differences in molecular orbitals of ZnPc and FePc, we can describe the different thickness-dependent molecular configuration, as well as core-level shifts. The stronger interaction of FePc with Au with respect to ZnPc can explain the smaller thickness-dependent shifts (C1s and N1s) for FePc. FePc receives electrons from Au, which enhances the screening of its core-level spectrm and decrease the thickness-dependent shifts. The discrepancy in X-ray absorption spectra points to a standing configuration of FePc molecules at the thick film, due to higher intermolecular interaction of FePc compared to ZnPc. Again the partially-empty d orbitals of Fe, can facilitate the molecular interaction and induce a standing molecular configuration in the thick film. This change of configuration and stronger intermolecular interaction indicate a higher electron conductivity within FePc molecules, also supporting the small thickness-dependent shift for FePc core-level spectra.

4.1.3. Tuning the hole barrier injection

In paper (II), the effect of adding a iodine layer as an intermediate layer between MPcs and Au(111) is investigated. A monolayer of each MPc was deposited separately on two Au-I surfaces. The two Au(111)-I surfaces are described in sec. 3.2.1. The core-level spectra from Au-I surfaces with and without MPcs are presented in Figure 4-1.4.
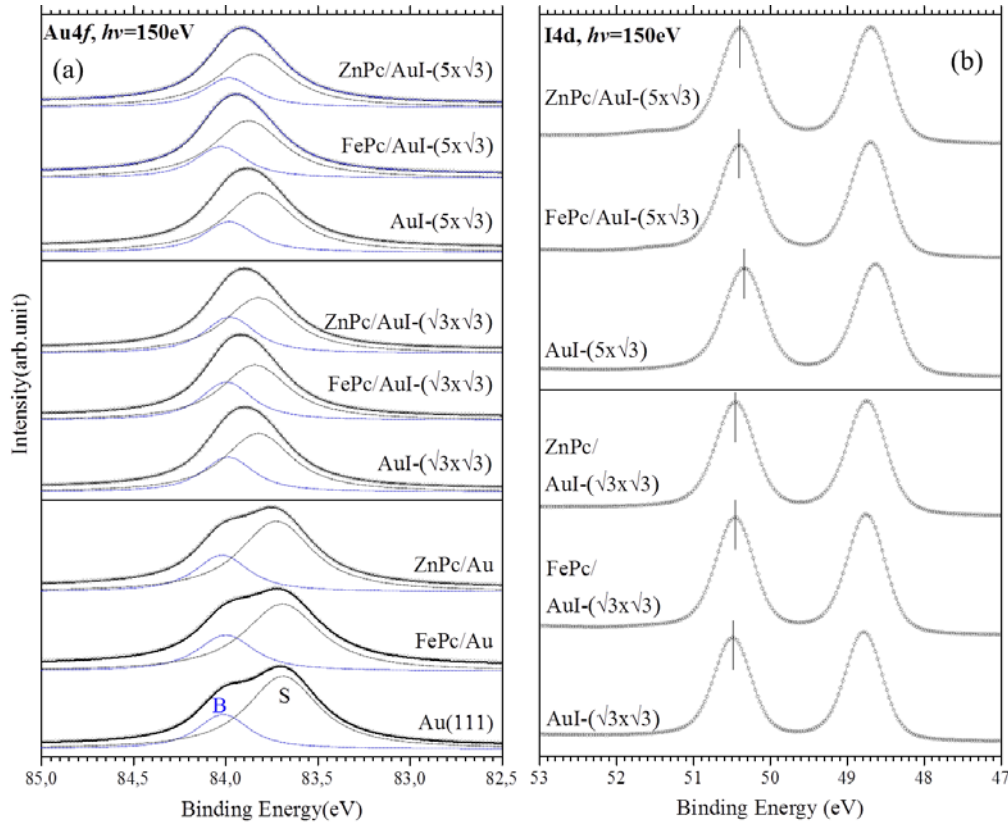
Figure 4-1.4: Photoemission spectra with numerical fits from Au(111) and Au(111)-I, with and without MPc; **(a)** Au4f$_{7/2}$ and **(b)** I4d.

Au4f$_{7/2}$ spectra (Figure 4-1.4(a)) look different under iodine layers. The surface shift which was 0.32 eV for Au(111) is changed to 0.16 eV upon iodine deposition. This shift is the same for both Au-I-$(\sqrt{3} \times \sqrt{3})$R30° and Au-I-$(5 \times \sqrt{3})$, which is in agreement with our calculations which showed that iodine reduces the charge density in the first gold layer. However adsorption of MPcs does not shift the surface peak further, similar to when they were adsorbed directly on the bare Au(111). In the panel (b) of Figure 4-1.4, I4d spectra are presented. There is no shift or line-profile variation due to adsorption of MPcs. However there is a slight shift (0.15 eV) between the iodine spectra of two different surfaces, which is explained by higher electron density on the iodine atoms in the compressed phase compared to the $(\sqrt{3} \times \sqrt{3})$ surface.

Near Fermi region of the valence band, including HOMO for monolayers of FePc and ZnPc is presented in Figure 4-1.5 (a) and (b) respectively. The 1ML spectra from FePc on $(\sqrt{3} \times \sqrt{3})$ and $(5 \times \sqrt{3})$ demonstrate a significant discrepancy with respect to the adsorption of the same layer on Au(111). On $(\sqrt{3} \times \sqrt{3})$, the shoulder just below the Fermi level which was assigned to the former LUMO is less intense and is shifted to lower BE. This peak disappears when FePc is adsorbed on $(5 \times \sqrt{3})$, indicating that this charge transfer channel is blocked on this surface.
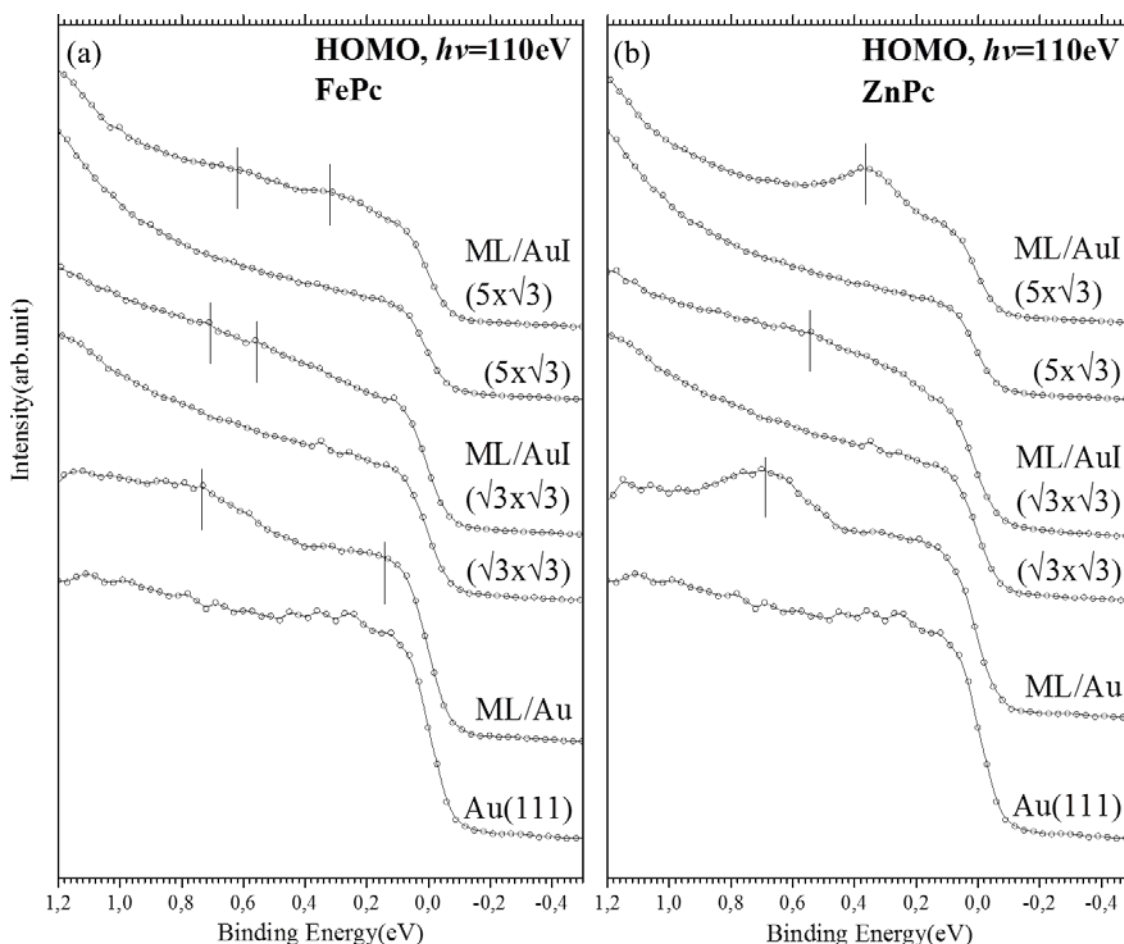
Figure 4-1.5: Near Fermi level region of the valence band photoemission spectra of **(a)** FePc and **(b)** ZnPc.

Figure 4-1.5 (b) shows the HOMO of a monolayer of ZnPc, adsorbed on Au and the two Au-I surfaces. The HOMO peak is centered at 0.69 eV on Au(111) and shifts to lower BE by 0.14 eV on $(\sqrt{3} \times \sqrt{3})$, and further to 0.36 eV on the $(5 \times \sqrt{3})$ surface. The shifts and positions of HOMO peak of ZnPc are comparable with the low-BE feature of HOMO peak of FePc. This resemblance point to the same origin for these two peaks, which is HOMO on the Pc-ring[59]. It was shown previously that FePc on Au(111) has contributions from both Fe-3d orbitals and Pc-HOMO, whereas ZnPc HOMO only contains Pc contributions[59]. In FePc, there are several Fe3d-derived orbitals which have about the same energy as the Pc-HOMO. It has been suggested previously that upon a perturbation in the

molecule, the order of these d-orbitals can change and the charge can redistribute in the FePc [59]. Knowing the origin of ZnPc HOMO and low-BE feature of FePc HOMO, we propose that the Pc-related HOMO shifts to lower BE due to increase of the surface electron density. These orbitals are not directly affected by central atom of the Pc. The high-BE feature of FePc which is assigned to Fe 3d-derived orbitals experience a minor shift compared to the shift of π orbitals. This small shift is explained by a reduced surface-Fe interaction in the presence of iodine layers. Therefore it is concluded that insertion of iodine layer increases the surface charge density, which results in the shift of HOMO and LUMO upwards. As a consequence of this shift the hole injection barrier in reduced by 0.33 eV (for Au-I-($5 \times \sqrt{3}$)).

4.2: ZnPc on Pt(111): structure, chemical interaction and charge transfer

4.2.1. The effect of substrate on the molecular growth mode

The electronic structure of ZnPc, from sub-monolayers to thick films, on Pt(111) are studied by means of XPS, XAS, and STM. Pt4f spectra from bare Pt(111) and also after ZnPc deposition are presented in Figure 4.2.1. Considerable reduction in intensity of the surface peak (S) upon adsorption of ZnPc, as well as appearance of a chemically-shifted component (C), points to a strong interaction between ZnPc and Pt(111) compared to e.g. Au(111).
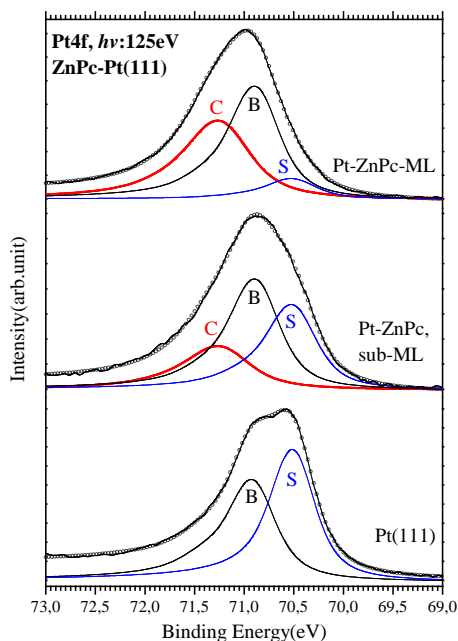

Figure 4.2.1: Pt4f spectra of ZnPc on Pt(111). B: bulk peak, S: surface peak, C: chemically-shifted peak.

Another interesting observation is that the surface peak is remained partially in the Pt4f spectrum, indicating some "untouched" surface areas. Kröger et.al.[73] showed previously for CuPc on Ag(111)

that molecules find their favorable positions based on their interaction with the substrate rather than intermolecular interactions. There is a substrate-mediated repulsive intermolecular interaction at the interface, which does not allow the molecules to pack tightly and cover the whole surface[73]. Our STM results confirm this type of growth for ZnPc on Pt(111) in sub-ML and ML regimes, shown in Figure 4-2.2 (a). Figure 4-2.2 (b), (c) and (d) are 330×350 Å^2, 900×540 Å^2 and 1800×1600 Å^2 respectively, illustrating the formation of a sponge-like structure at higher coverage. The observed holes (dark rings) represent the surface areas which are not covered by ZnPc, in agreement with the presence of the Pt4f surface peak in coverages higher than 1 ML.
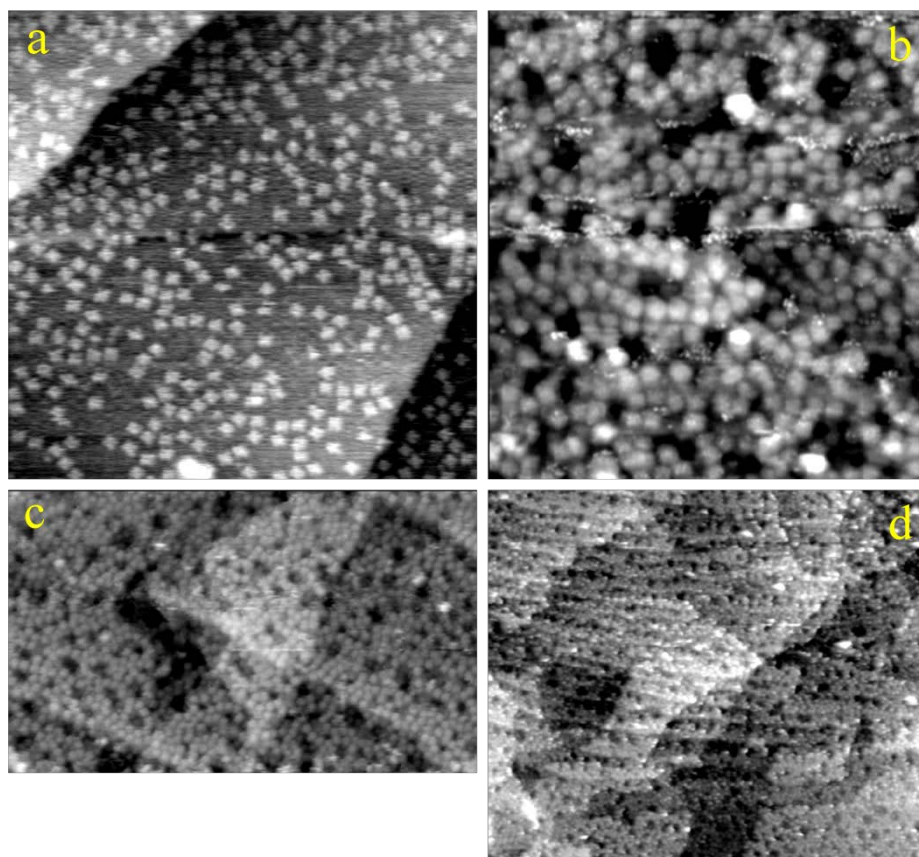
Figure 4-2.2: Room temperature STM images of ZnPc on Pt(111); **(a)** Sub-ML of ZnPc/Pt(111); 360x360 Å^2, 60 pA, 125 mV, and multilayer of ZnPc/Pt(111): (b) 330x350 Å^2, 68 pA, 9 mV, **(c)** 900x540 Å^2, 68 pA, 125 mV **(d)** 1800x1600 Å^2, 0.8 nA, 53 mV.

Our NEXAFS results (not shown here) suggest a flat lying molecular configuration at the ML, and a tilted orientation ($\varphi < 45°$) in the thick film. Flat molecules at the lower coverages can be seen in the STM images but there is no high-coverage STM image, illustrating the tilted molecules on the surface.

4.2.2. Substrate-induced inhomogeneous charge transfer

Photoemission spectra of C1s, N1s and Zn3d are presented in Figure 4-2.3 (a), (b) and (c) respectively. C1s spectrum from sub-ML of ZnPc on Pt(111) looks very different from the molecular thick film. This considerable disturbance at the interface is due to the strong interaction between ZnPc and Pt. Results of curve-fitting indicate the coexistence of two C1s peaks; the one in lower BE from the interface molecules and the other from the "bulk-like" molecules. In the TF spectrum only the higher BE components are present and shake-up structures are also visible.
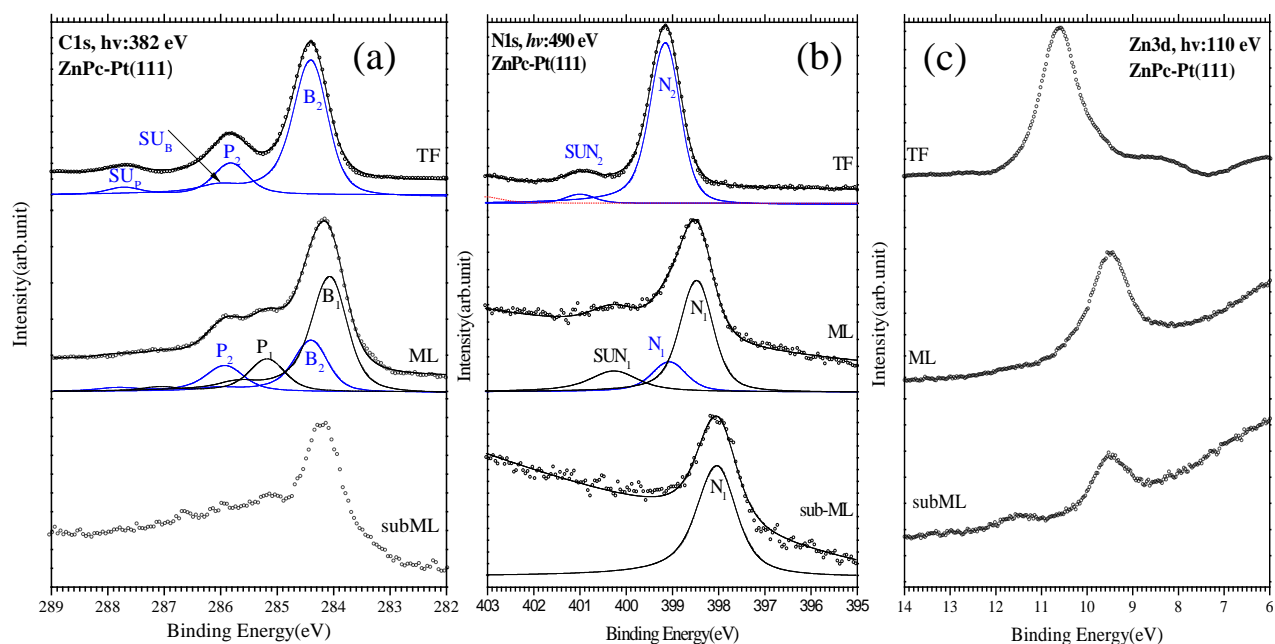
Figure 4-2.3: **(a)** C1s, **(b)** N1s and **(c)** Zn3d photoemission spectra of ZnPc on Pt(111).

N1s and Zn3d spectra in Figure 4-2.3(b) and (c) illustrate the same effect. There are coverage-dependent shifts for each group of atoms; ΔC_B: 0.32 eV, ΔC_P: 0.75 eV, ΔN: 0.65 eV and ΔZn: 1.1 eV. Variations in coverage-dependent shifts were reported before and indicate inhomogeneous charge transfer and/or core-hole screening for different atoms[21,61,68].

On the other hand, C and N peaks have higher binding energies compared to when they are adsorbed on Au(111), while Zn3d has a lower BE on Pt(111). Therefore it is fair to conclude that charge transfer at the interface between ZnPc and Pt is inhomogeneous. Previously this inhomogeneous charge transfer was assigned to a non-planar molecular configuration. It is suggested here that ZnPc is also bent on Pt(111), i.e., Zn is protruding out towards the surface and the organic rings are bent upward.

4.2.3. ZnPc adsorption on Pt(111)-I surfaces

Adsorption of iodine on Pt(111) leads to two different reconstructions: $(\sqrt{3} \times \sqrt{3})$, at 1/3 ML and $(\sqrt{7} \times \sqrt{7})$ at 3/7 ML iodine coverage. On $(\sqrt{3} \times \sqrt{3})$, iodine occupies hollow sites. Adsorption energy calculations have not been able to tell the fcc and hcp hollow sites apart on $(\sqrt{3} \times \sqrt{3})$. In $(\sqrt{7} \times \sqrt{7})$, both of them have been suggested to be occupied together with the top site .

There are no observable peak shifts or changes in the relative intensity of Pt4f spectra from either of the surfaces upon ZnPc adsorption, indicating that ZnPc does not affect Pt in the presence of iodine intermediate layer.

Molecular configuration

X-ray absorption spectra from ZnPc ML on both Pt(111)-I surfaces, presented in Figure 4-2.4 point to a flat-lying molecular configuration. ZnPc molecules show a tilted orientation in the thick film on $(\sqrt{3} \times \sqrt{3})$, however they remain flat lying on the $(\sqrt{7} \times \sqrt{7})$ surface. The origin of the tilt of ZnPc film on the $(\sqrt{3} \times \sqrt{3})$ surface is described as weaker molecule-substrate interaction at this surface, compared to two other surfaces.
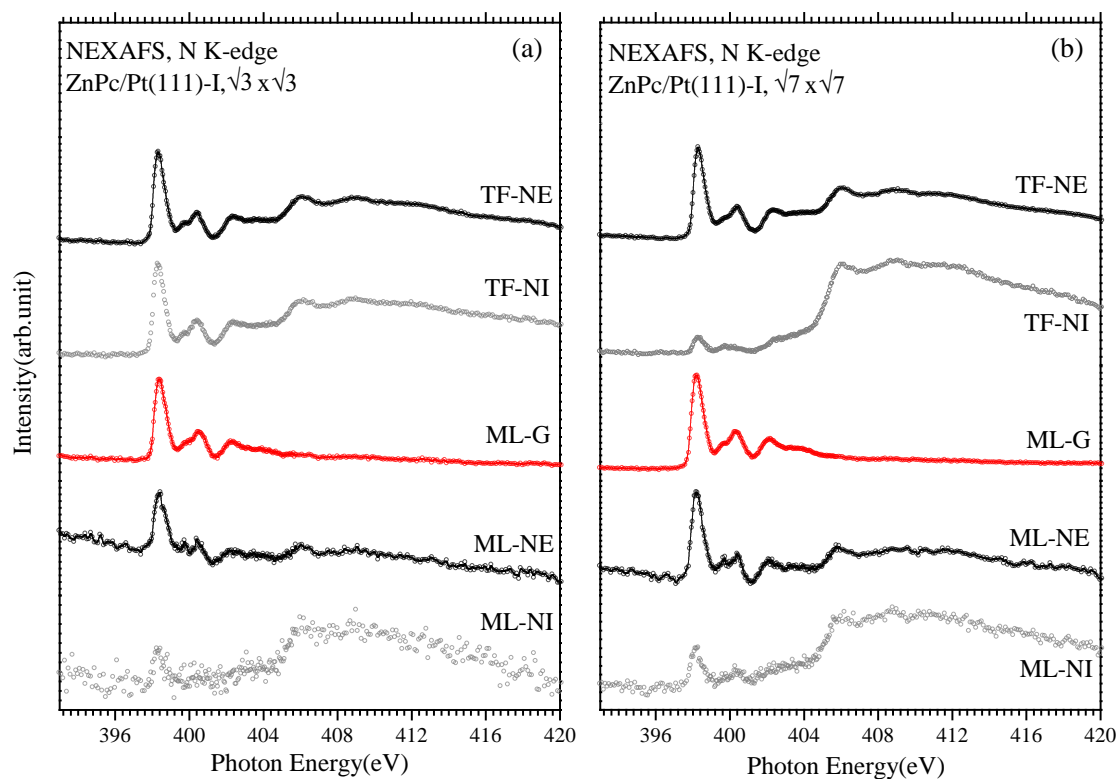

Fig.4-2.4: N-K edge NEXAFS spectra of monolayers and thick films of ZnPc on **(a)** PtI-$(\sqrt{3} \times \sqrt{3})$ and **(b)** PtI-$(\sqrt{7}\sqrt{7})R19°$.

Zn3d

Zn3d from 1ML of ZnPc on $(\sqrt{3} \times \sqrt{3})$ is located in higher BE compared to Pt(111), indicating to reduced charge transfer from substrate to Zn. Besides, there is no coverage-dependent shift in Zn3d spectra as depicted in Figure 4-2.5(a), implying a weak interfacial interaction. When ZnPc is adsorbed on Pt(111)I-$(\sqrt{7} \times \sqrt{7})$, Zn3d from ML also appears at higher BE with respect to ZnPc/Pt(111), although slightly lower than on $(\sqrt{3} \times \sqrt{3})$ surface. As presented in Figure 4-2.5(b), there is a coverage-dependent shift on $(\sqrt{7} \times \sqrt{7})$. This shift (0.47 eV) is smaller than what was observed on Pt(111) (1.1 eV).
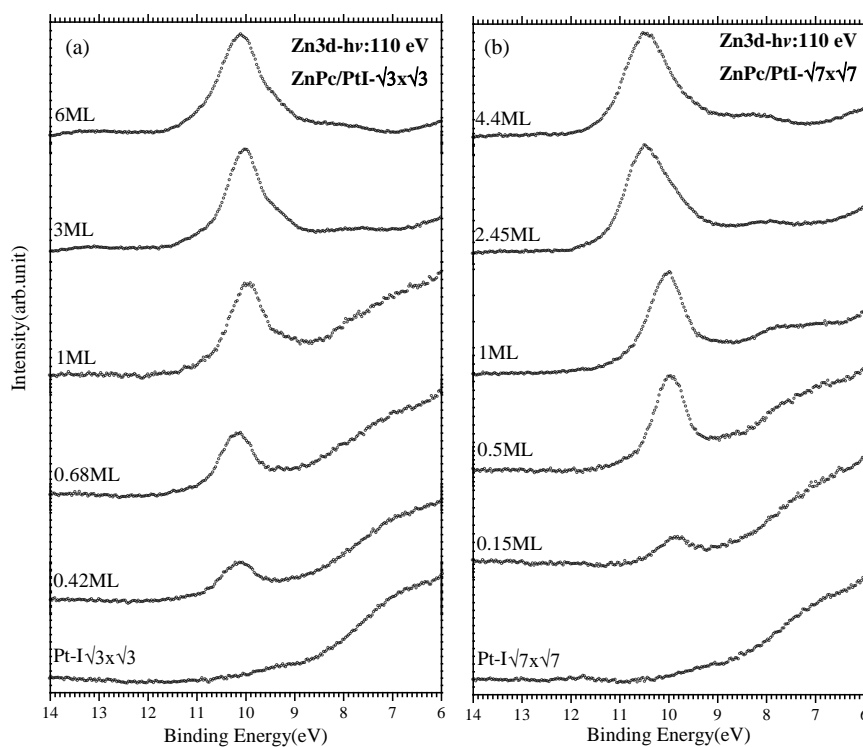
Figure 4-2.5: VB spectra of ZnPc layers on **(a)** PtI-$(\sqrt{3}\times\sqrt{3})$R30° and **(b)** PtI-$(\sqrt{7} \times \sqrt{7})$.

C1s and N1s

C1s and N1s spectra from ZnPc on PtI-$(\sqrt{3} \times \sqrt{3})$ in Figure 4-2.6 (a) and (b) demonstrate that they can be fitted with only one component, meaning that there is no component induced by the interfacial interaction. Opposite to Zn3d, binding energies of both C1s and N1s at ML are slightly lower than their corresponding BEs on Pt. However, no coverage-dependent shift is observed for the sets of C1s and N1s spectra, confirming the weak interaction at the interface.

Figure 4-2.6 (c) and (d) present C1s and N1s spectra from ZnPc on PtI-$(\sqrt{7} \times \sqrt{7})$. The binding energies at ML are marginally lower than the ones on PtI-$(\sqrt{3} \times \sqrt{3})$. However there are considerable

line shape differences compared to PtI-$(\sqrt{3} \times \sqrt{3})$; both C1s and N1s comprise chemically-shifted components. The direction of these shifts implies the charge transfer from substrate to ZnPc. Furthermore there are thickness-dependent shifts; ΔC_B: 0.52 eV, ΔC_P: 0.57 eV, ΔN: 0.52 eV and ΔZn: 0.47 eV. We conclude that the charge transfer at PtI-$(\sqrt{7} \times \sqrt{7})$ is stronger than on $(\sqrt{3} \times \sqrt{3})$ and weaker than on Pt(111). A more crucial conclusion which can be drawn is that for both Pt-I surfaces, the charge transfer at the interface is more homogeneous than on Pt(111). The origin of the strong ZnPc-Pt(111) interaction is mediated by the central atom (Zn), leading to a non-planar molecular configuration. Insertion of iodine between Pt and ZnPc, reduces the interaction and causes a more even charge distribution within the molecules and consequently a more "flat" molecular plane.
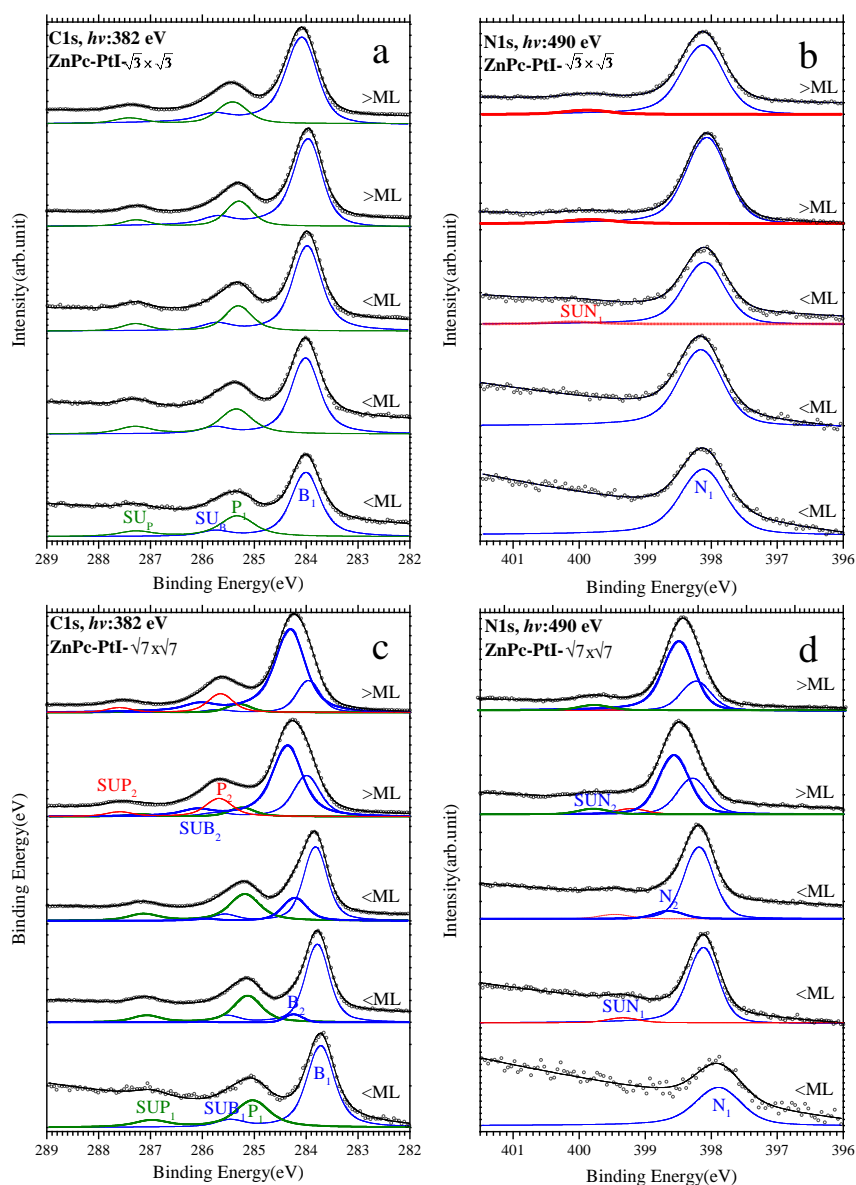

Figure 4-2.6: (a) C1s spectra and **(b)** N1s spectra of ZnPc layers on PtI- $(\sqrt{3}\times\sqrt{3})$R30° ; **(c)** C1s spectra and **(d)** N1s spectra of ZnPc layers on PtI- $(\sqrt{7}\times\sqrt{7})$R19°.

4.3: Adsorption of ZnPc on TiO$_2$(110)

4.3.1 Charge transfer at the interface

Contribution of the d-orbital of transition-metal phthalocyanine is crucial in the charge transfer phenomena between MPc and oxide substrates. In order to get a clear image of interaction between organic ligands and the substrate, ZnPc layers on TiO$_2$ are studied. The fact that Zn, having a fully filled d orbital is located deep below the organic frontier orbitals enables us to investigate more on the role of organic ligands in the interfacial interaction.

Selected core level spectra of C1s and N1s from ZnPc on TiO$_2$ are presented in Figure 4-3.1. Curve fitted spectra are also included to better illustrate the different components of each spectrum. These spectra demonstrate that two adsorption modes are coexisting already at the sub-monolayer region, indicating island growth. These two adsorption modes belong to either interfacial molecules or more bulk-like molecules. According to the gradual development of peaks, the higher binding energy components are assigned to interfacial molecules, whereas the peaks at lower BE side represent bulk-like molecules, which are not in direct contact with the substrate. This is in agreement with theoretical studies, predicting a charge transfer from Pc to TiO$_2$[100,101].
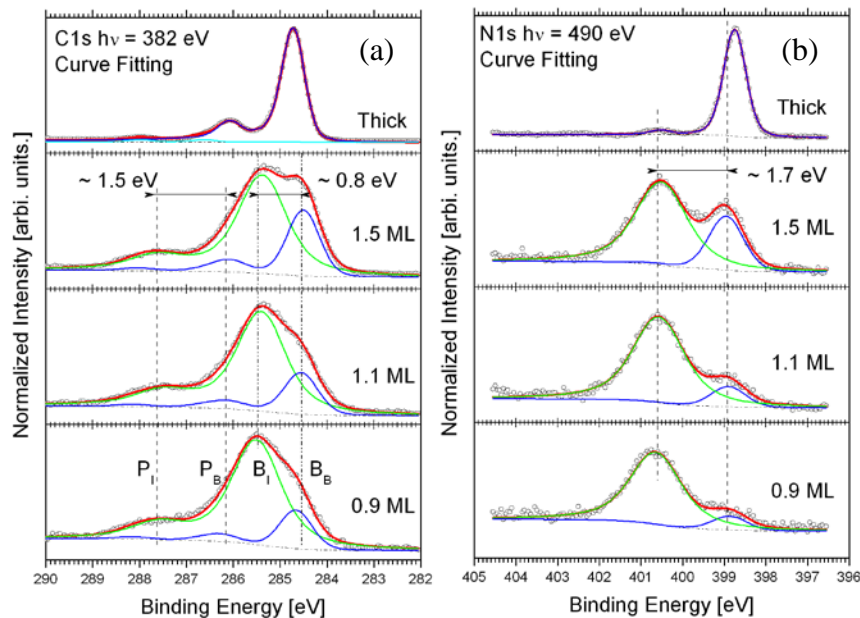
Figure 4-3.1: Selected curve fitted spectra **(a)** C1s and **(b)** N1s. B$_I$ and P$_I$ represent benzene carbon and pyrrole carbon atoms of interfacial molecules respectively. B$_B$ and P$_B$ represent the counterparts on bulk-like molecules. The energy level alignment is guided with dot lines. In the C1s spectra (c), the shift between P$_I$ and P$_B$ is about 1.5 eV, while that of B$_I$ and B$_B$ is 0.8 eV. In N1s spectra, the shift between interfacial state and bulk like state is around 1.7 eV.

An interesting observation is the thickness-dependent core level shifts. Different atoms of ZnPc respond differently to increase of coverage from ML to TF. Based on our curve-fitting results, the gap between C_B in the monolayer and thick film is 0.8 eV, while this difference is 1.5 and 1.7 eV for C_P and N respectively. Discrepancy in the gap between interfacial and bulk-like molecular layers is due to different electronic environment around each atom. These shifts are generally explained by initial and final state effects. Since, the inner atoms (C_P and N) experience larger shifts, it is fair to say that the central part has lower charge density and/or is less screened than the outer part. Zn3d spectra (not shown here) showed two components also. The shift between two components of Zn3d is smaller than C1s and N1s, in agreement with the suggested picture. Besides, our calculations propose that by changing the charge distribution of the molecule, Zn will be influenced the least, since it is moderated by the electron density of the organic ligands. Similar observation was reported before by Giovanneli *et al*[102].

4.3.2. d-orbital

The inhomogeneous charge transfer screening is valid for ZnPc on TiO_2, while a more even one was reported for FePc on TiO_2. The reasons for this inhomogeneity are summarized as following; 1) open shell Fe d−orbitals contribute to the HOMO and participate in interactions with the substrate or doping. However, the zinc metal center with filled d-orbitals is rather inert compared to Fe and is less influenced by changes in the peripheral part of the molecule. The possible Pc-orbital hybridization through the central atom, which may generate different screening for interface molecules depend on the central metal atom. 2) Molecular tilt angle (30° for ZnPc) may block the direct contact between Zn and substrate. Whereas, smaller angle reported for FePc, may facilitate this hybridization. 3) Shorter theoretically calculated bond length for FePc (Fe-N~ 1.92 Å) with respect to ZnPc (Zn-N~ 1.98 Å) may intrinsically influence the screening.

4.3.3. NEXAFS

X-ray absorption spectra are measured at the N K-edge and C K-edge, which are presented in Figure 4-3.2. Similar to core level spectra, absorption spectra show different components for molecules at the interface and bulk-like molecules. The gap between interfacial contributions and bulk-like ones in NEXAFS are smaller than the gaps observed in core level spectra; the gaps in NEXAFS are almost of the same size for different components. Since the observed thickness-dependent shifts in NEXAFS correspond to initial state effects, while the shifts in XP spectra correspond to both initial and final state effect, the inhomogeneous thickness-dependent shifts for different atoms is assigned to different

charge transfer screening of the interface layer via the substrate. Accordingly we can conclude that a core excited benzene carbon is better screened by charge transfer from the substrate than a pyrrole one.

4.3.4. Lifetime of a core excited state

Another significant observation from C1s and N1s core level spectra (Figure 4-3.1) is in the Lorentzian width of different peaks. We observe larger Lorentzian widths for interfacial components than the bulk components. Lorentzian width corresponds to the lifetime of the core excited state, i.e., a larger Lorentzian width points to a shorter lifetime. Hence, it is suggested that the core excited state has a shorter lifetime in the interfacial molecules than the bulk molecules.
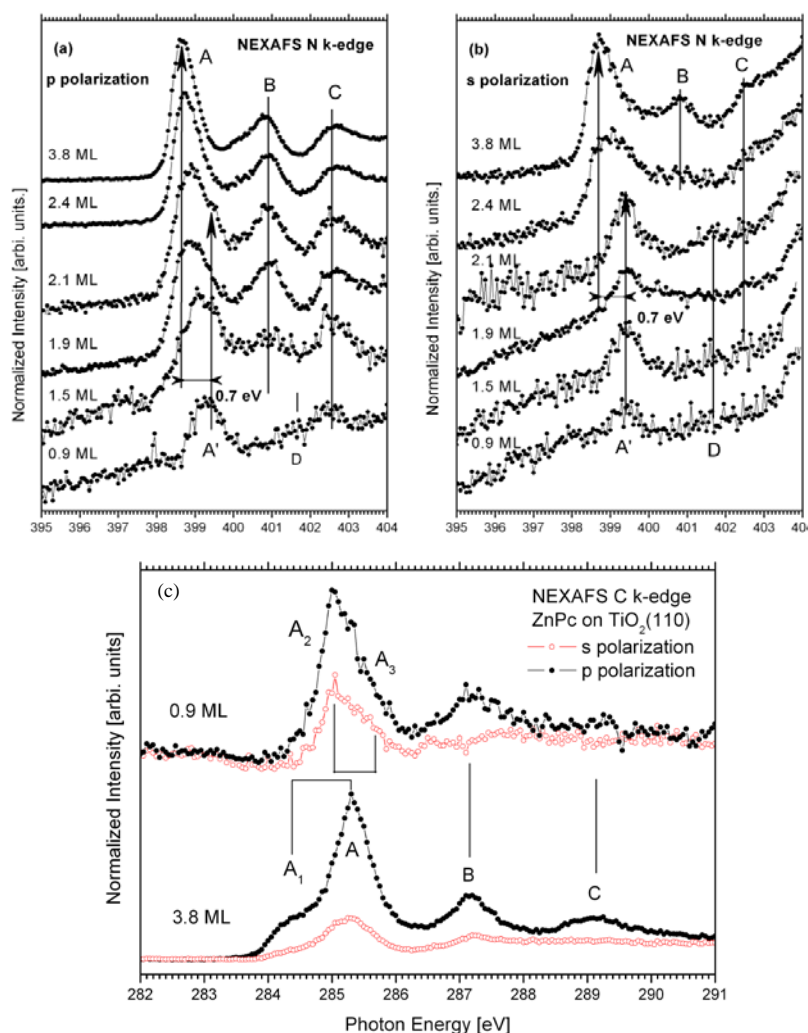
Figure 4-3.2: (a) p polarization and **(b)** s polarization NEXAFS spectra at different coverage under. A and A´ stand for the first resonant transition from N1s to LUMO in bulk like molecule and interfacial molecule, respectively. Transition B and C of the bulk like molecule and transition D of the interfacial state molecule represent the transition from N1s to higher empty orbital π^*. **(c)** C K-edge NEXAFS spectra from 0.9 ML (top) and 3.8 ML (bottom). Spectra collected under p and s polarization are plotted with black solid dot line and red void line. A and A_1 are the transition from C_B and C_P to LUMO for the bulk like molecule, while A_2 and A_3 are attributed to the C1s transition to LUMO for the interfacial state. Transition B and C stem from the excitation from C1s to higher empty π^* orbital.

4.4: Adsorption of MgPc on TiO$_2$(110); (1×1) and (1×2)-cross linked structures

The TiO$_2$(110) surface can exist in different structures; (1×1), (1×2) and (1×2)-cross linked. Ball models based on previous work of these three structures are shown in Figure 4-4.1. Large balls represent oxygen and small balls are titanium. On (1×1), the yellow oxygen and the grey titanium are in the same plane, while the orange oxygen is in bridge site on the Ti, sticking out from the surface. On (1×2), the brown oxygen and the blue titanium form an added row structure with Ti$_2$O$_3$ stoichiometry. The cross-linked surface is formed by breaking the (1×2) rows and shifting a group of atoms along $[1\bar{1}0]$ into the channels between the (1×2) rows. Crystal directions are indicated by arrows.
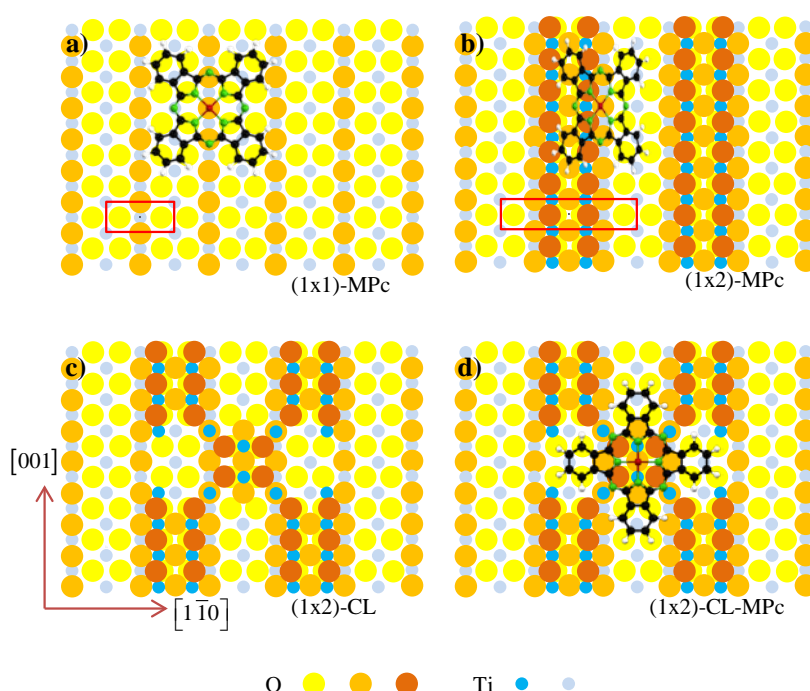
Figure 4-4.1: Top view atomic models of three different surface terminations on rutile TiO$_2$(110); (1×1), (1×2) and cross-linked (1×2). Small balls represent Ti and large balls are oxygen. Crystal directions and unit cells are indicated by arrows or red rectangles. The unit cells are 3.1Å x 6.35Å for (1x1) and 3.1Å x 12.7Å for (1x2)-CL. Phthalocyanine molecules are also added to the surfaces; with a red central atom, green nitrogen, black carbon and white hydrogen.

Upon adsorption of MgPc, the metal ion is centered on top of an oxygen atom and the benzene rings are arranged between the oxygen rows. When MgPc is adsorbed on a (1×2)-CL, there are two possible positions for MgPc. If MgPc is adsorbed on the cross-linked part, it lies flat (Figure 4-4.2(b)). However, visible from the same STM image, the neighboring molecules look smaller compared the circled molecule, implying a tilted orientation on the added rows.

Figure 4-4.2: STM images from the (1×2) cross linked surface, **(a)** 380x560Å^2 (+3.0V, 254 pA) from the clean surface **(b)** and 235x250Å^2 (+1.7V, 30 pA) with a monolayer of MgPc.

4.4.1. Thick film
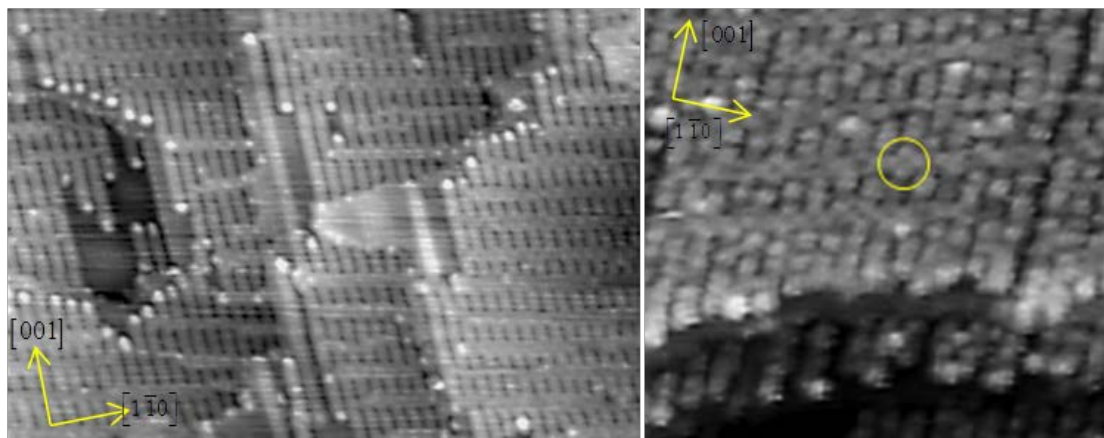
XPS and NEXAFS from C and N of the thick film of MgPc on TiO$_2$ surface showed molecular spectra as observed before for different MPc thick films[21,39]. Investigations on XA spectra showed that line profile of N K-edge spectrum is more influenced by the central atom compared to C K-edge spectrum, due to the direct binding of half of nitrogen atoms to the metallic center.

4.4.2 Low coverage

In Figure 4-4.3, N1s and C1s spectra from low coverage MgPc on TiO$_2$ (1×1) and (1×2)-CL are presented. All low-coverage spectra contain both an interface component and a "bulk-like" component. The energy separations between these two components for different spectra are summarized here. $\Delta E_N(1 \times 1) = 1.7$ eV, $\Delta E_{CB}(1 \times 1) = 0.7$ eV, $\Delta E_N(1 \times 2) = 1.8$ eV and $\Delta E_{CB}(1 \times 2) = 0.8$ eV. Variation in the chemical shift for different atoms points to an inhomogeneous charge transfer at the interface observed before for ZnPc adsorbed on TiO$_2$[21]. Even though, the N$_I$ chemical shifts are almost the same, there is a difference between C$_P$ shifts as well as their position for the different substrates, which is originated by their different positions on the surfaces, resulting in a different electronic environment and final state screening possibilities.

NEXAFS results from the low-coverage MgPc on TiO$_2$ surface (not shown here), show that there are reacted and un-reacted molecules on both (1×1) and (1×2)-CL. The first layer on (1×1) is tilted. Its LUMO-related first XAS peak is shifted from the first resonance of the un-reacted molecules by 0.9 eV. The un-reacted second layer is lying parallel to the surface. On (1×2) un-reacted molecules are standing on the surface as-deposited.
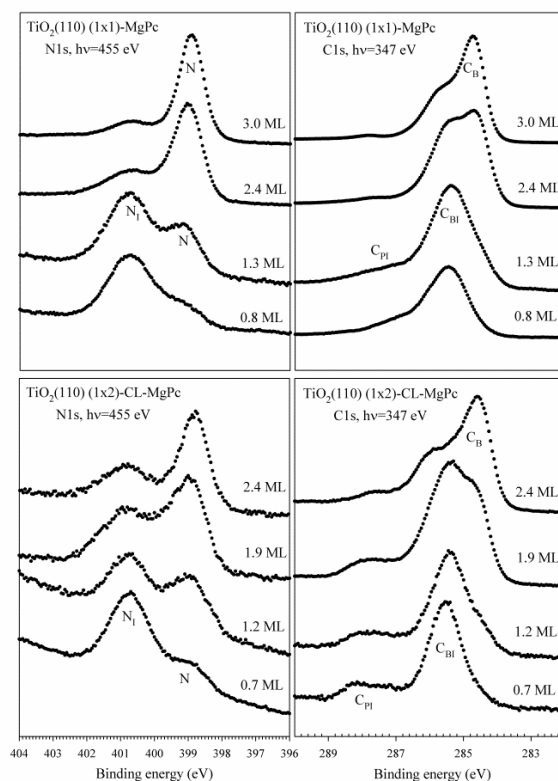
Figure 4-4.3: N1s and C1s spectra recorded from thin MgPc layers on (1×1) and (1×2)-CL.

The near-Fermi region spectra are shown in Figure 4-4.4. Positions and the line shape of HOMO peaks of the second layer are different on different substrates. Modification of the substrate with intermediate layers as well as molecular configuration influence the interface dipole[38,103]. Our results point to a discrepancy in interface dipole, which is induced by different electronic structure of the two surfaces, as well as various molecular configurations at these surfaces.
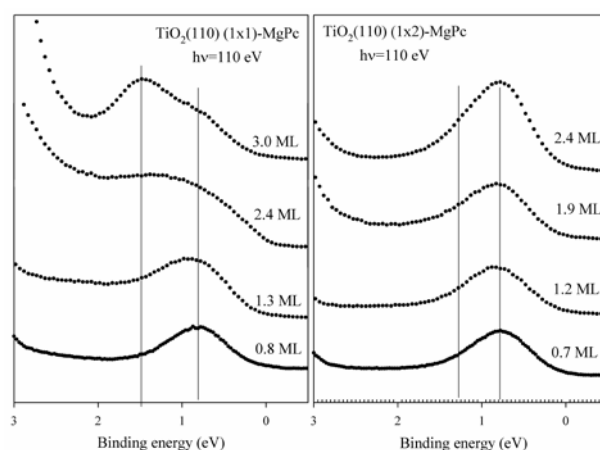
Figure 4-4.4: Photoemission spectra from the HOMO region recorded from monolayer films on the (1×1) and (1×2)-CL surfaces.

4.4.3. Band bending

O1s spectra from both surfaces with and without MgPc are presented in Figure 4-4.5(a) and (b). The peaks are single-component, representing both surface and bulk atoms. Shift of the whole spectrum to higher BE (0.25 eV) indicates a downward band-bending on the (1×1) surface after MgPc adsorption, which is nicely supported by Ti2p spectra.

Our heat treated TiO_2 sample is conductive and an n-type semiconductor with the Fermi level 3.0 eV above the valence band edge. Given that the band gap is 3.2 eV, the Fermi level is 0.2 eV below CBM. After MgPc adsorption the Fermi level is above CBM and the surface becomes metallic with a small charge accumulation layer in the sub surface region. On the other hand, no band bending is observed when MgPc is adsorbed on (1×2)-CL. The binding energy of O1s and Ti2p on TiO_2 (1×2)-CL are at the same position as their respective spectra on (1×1) after MgPc adsorption. Therefore, the Fermi levels are at the same energy with respect to the band edges, which means that the (1×2)-CL surface is already metallic before adsorbing MgPc. The additional charge from the monolayer of MgPc does not suffice to shift the Fermi level further up in the conduction band.
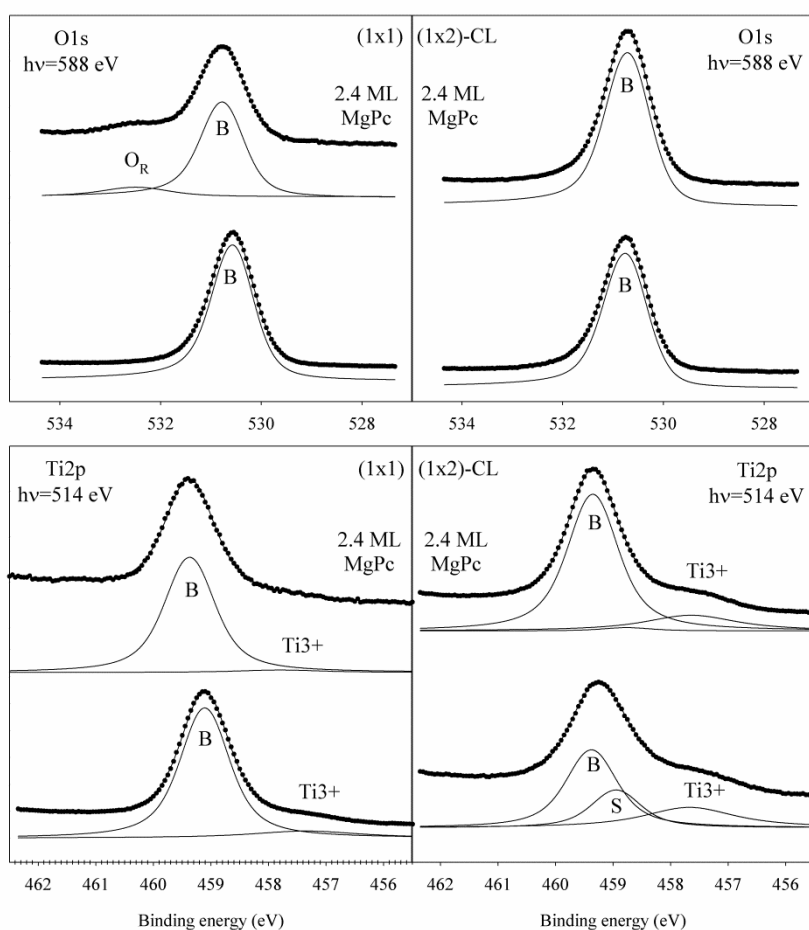

Figure 4-4.5: O1s and Ti2p spectra recorded from $(\mathbf{1 \times 1})$ and $(\mathbf{1 \times 2})$-**CL** with and without MgPc.

4.5: 4TBP on Pt(111): Dissociative bonding

Room temperature adsorption of 4TBP on Pt(111) is studied by XPS, NEXAFS and density functional theory (Paper VI). Figure 4-5.1, shows the optimized adsorption geometry of 4TBP on Pt(111), which illustrate that 4TBP is attached to the substrate with N and a neighboring carbon to three Pt atoms. This adsorption dissociatively breaks the C-H bond and the hydrogen atom remains in a top-site. The saturation coverage at room temperature is 0.2 ML, leaving 0.2 ML of the surface atoms, free from adsorbates (since four Pt atoms are engaged with one 4TBP molecule.). Our NEXAFS spectra suggested an almost up-right configuration of the molecule on Pt(111) (~72°), which is in reasonable agreement with the theoretically predicted orientation. N1s peak from the 4TBP layer on Pt(111) is centered at 399.2 eV, close to reported values for N-containing adsorbates on Pt(111) and NH (399.0 and 399.7 eV respectively)[104], confirming the N-Pt bond.

Pt 4f spectra from the clean Pt surface and under 4TBP are presented in Figure 4-5.2(a). In the clean substrate spectrum, there are two peaks; S peak represent the surface atoms and B peak represent Pt atoms from the bulk. The surface shift is 0.41 eV in agreement with literature[105,106]. Upon adsorption of 4TBP, as shown in Figure 4-5.2 (a), two more peaks develop on expense of the surface peak. The sum of integrated area of two chemically-shifted peaks (C and H) and S is almost of the same size as S on the clean surface. Relative intensity of the S peak is 11% at the saturation coverage, which is 1/5 of its intensity in the clean Pt spectrum, pointing to the fact that 1/5 of Pt atoms are not influenced by adsorption of 4TBP.
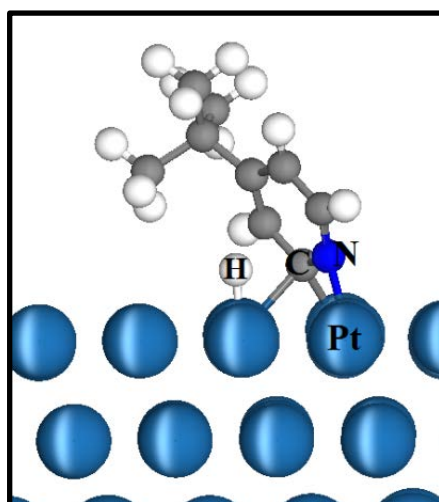

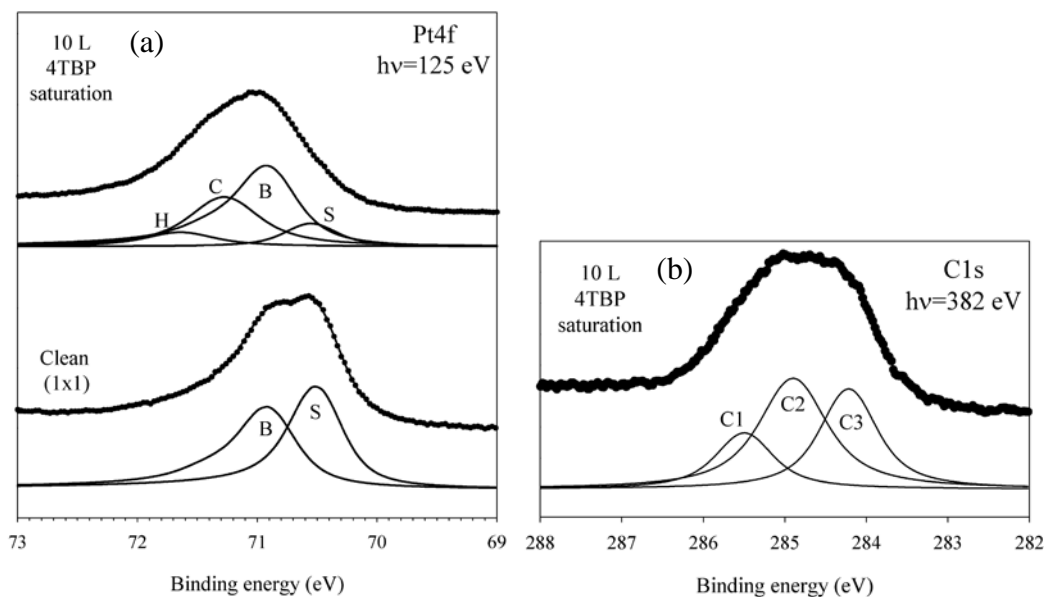**Figure 4-5.1:** Optimized adsorption geometry from DFT.

Figure 4-5.2: (a) Pt4f spectra from clean Pt(111) and and after saturation of the surface by 4TBP. **(b)** C1s spectrum from saturated layer of 4TBP on Pt(111).

C1s spectrum of saturated layer of 4TBP on Pt(111) in Figure 4-5.2 (b) consists of three peaks. From the molecular configuration on Pt, given in Figure 4-5.1, C atoms can be classified in three groups; butyl carbons (4 atoms), pyridine ring carbons (4 atoms) and pyridine carbon which is bound to Pt (1 atom). From the relative intensities presented by C1s curve-fitted spectra, C1 can be assigned to the C which is bound to surface. C2 and C3 are separated from each other by 0.68 eV and according to our calculations, C2 represent pyridine carbons and C3 is assigned to butyl carbons.

4.6: 4TBP on TiO$_2$(110); Bond site and band bending

4 tert-butyl pyridine (4TBP), which is an important additive to the redox electrolyte in dye-sensitized solar cells, is adsorbed on a single crystalline TiO$_2$(110). In this study, the effect of 4TBP adsorption on defect state of TiO$_2$ is studied using XPS and DFT calculations (Paper VII).

Ti2p$_{3/2}$ and O1s spectra from clean substrate and under different layers of 4TBP are presented in Figure 4-6.1(a) and (b) respectively. Our sample preparations cause reduction of the sample and consequently creation of oxygen vacancies in the oxygen rows. This will create Ti^{3+} under the missing oxygen. Ti^{3+} shows up as a hump in the lower BE side of the main Ti2p$_{3/2}$ peak. The main peak of Ti2p$_{3/2}$ spectrum represents Ti^{4+} (5-coordinated Ti at the surface and bulk Ti ions). Upon 4TBP adsorption, there are two significant observations; disappearance of the Ti^{3+} peak and the shift of both Ti2p$_{3/2}$ and O1s to lower BE by 0.15 and 0.2 eV respectively. Vanishing of Ti^{3+} peak, already at 0.02 ML adsorption of 4TBP, indicates that the oxygen vacancy is the preferred bond site for 4TBP molecules, also reported for 4-methylpyridine on TiO$_2$[107].
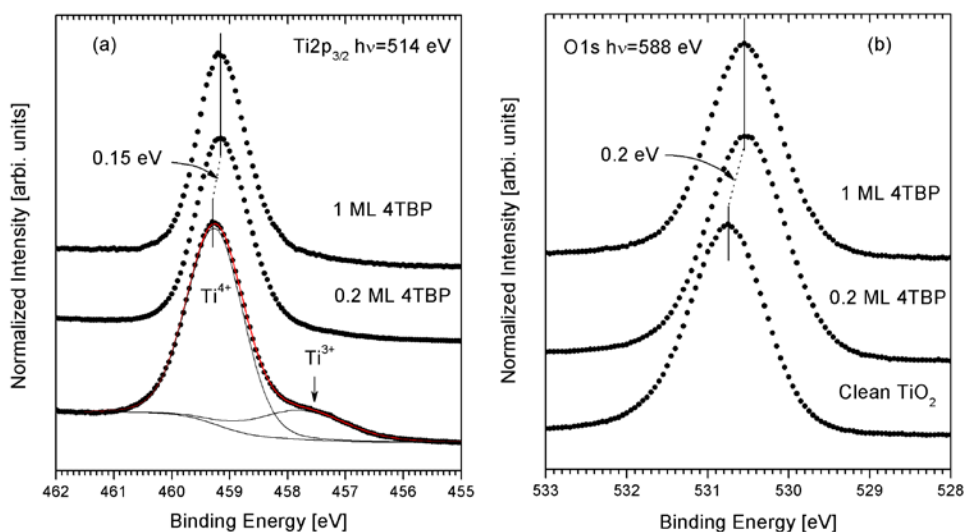
Figure 4-6.1: Ti2p **(a)** and O1s **(b)** spectra from $TiO_2(110)$ after different preparations.

For binding energy shift to lower BE, from clean surface to 1ML (saturated layer), one could think of chemical shifts, however presence of this shift already at 0.02 ML, suggest an adsorption-induced band bending (shift of the band edges). As illustrated in Figure 4-6.2(a), there is a surface state at about 1 eV below Fermi level, which corresponds to nonbonding Ti3d electrons at oxygen vacancies. This state was reduced due to adsorption of 4TBP and since the reduction of surface state intensity is more pronounced than the rest of the spectrum, it confirms the preferred 4TBP bond site, which is also supported by our calculations.
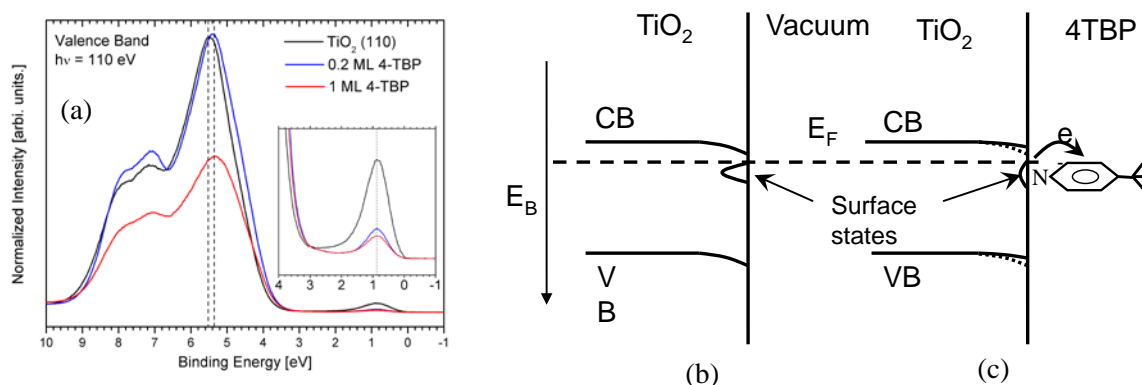
Figure 4-6.2: (a) Valence band spectra from the $4TBP/TiO_2$ interface compared with that of clean sample. Inserted image is the enlarged part of the VBM and surface state. Schematic illustration of the charge transfer and band bending **(b)** before and **(c)** after 4TBP adsorption. Dash line is Fermi level (E_F). CB and VB are conduction band and valence band, respectively. Dot lines in **(c)** are reproduced from the band edge of **(b)** to highlight the band shift. Arrows are indicating the direction of charge transfer.

On the other hand, results of C1s and N1s (not shown here) demonstrate no BE shift for N1s, while C1s experience a shift to higher BE upon 4TBP adsorption. The single N1s peak, which does not undergo any coverage-dependent shift, indicate a homogenous adsorption geometry; our calculations

also point to an up-right configuration, in which N is bonding to Ti, as demonstrated in Figure 4-6.3(a) and (b). Besides, absence of coverage-dependent shifts in N1s spectra proves that nitrogen does not play the role of either electron donor or acceptor. Thus it is not the reason for observed band bending.

As shown in Figure 4-6.2(b), upon heat treatment and formation of oxygen vacancies, substrate becomes n-type and a downward band bending is expected. By adsorption of 4TBP, the electrons from the surface state migrate to the molecules. Since nitrogen does not participate in this charge transfer, electrons from surface state end up in the pyridine ring. Figure 4-6.3(b) demonstrates that N penetrates in to the vacancy, enabling the molecular π^* to hybridize with the Ti3d orbitals. This explains the presence of coverage-dependent shifts in C1s spectra.

Typical density of oxygen vacancies in a good surface is ~ 8%, meaning that the dominant adsorption site for 4TBP on this surface is Ti rows (Ti^{4+}). Ti in these rows have less additional charge compared to oxygen vacancies, resulting in higher BE of C1s spectra in 1ML compared to sub-monolayer spectra.
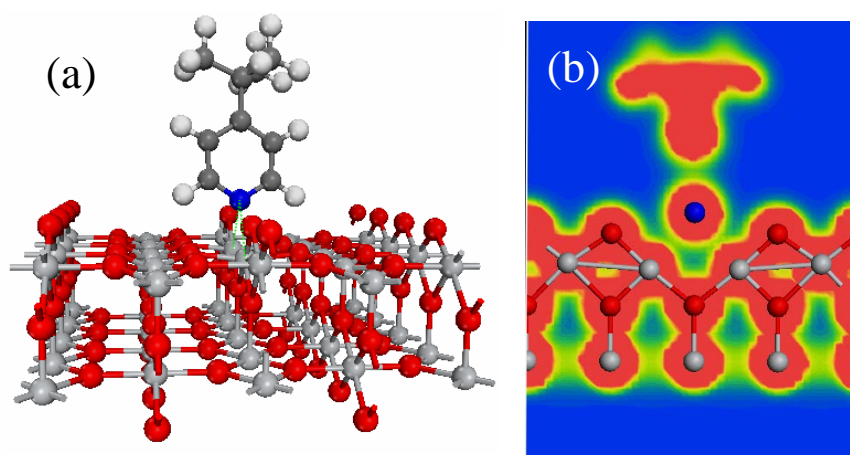

Figure 4-6.3: (a) Optimum geometry in the vacancy given by the calculations.
(b) Calculated charge distribution Oxygen, titanium and nitrogen are indicated by red, white and blue spheres. Red, yellow and blue areas in the distribution map label the high, medium and low density of electrons. Nitrogen binds with two neighbouring titanium atoms, as indicated by the black arrows.

Chapter 5

Conclusion and future work

The research work presented in this thesis is focused on synchrotron-radiation-based spectroscopy methods as well as STM, both conducted in UHV. The experiments were carried out using three different MPcs (M: Fe, Zn, Mg) adsorbed on three different substrates; Au(111), Pt(111) and TiO$_2$(110). The molecular configuration in various coverages as well as the charge transfer at the interface was studied. Besides, experiments on 4TBP adsorption on Pt(111) and TiO$_2$(110) were performed.

Moreover, the effect of iodine as an intermediate layer on Pt and Au as well as the influence of different surface reconstructions on TiO$_2$(110) was also investigated.

- Monolayers and thick films of MPc (M: Fe, Zn, Mg) are adsorbed on Au(111), Pt(111), TiO$_2$(110) 1×1 and 1×2-cross-linked. General charge transfer is observed for MPc adsorbed on Au(111) and TiO$_2$(110) to be from molecules to the substrate. However, when MPc was adsorbed on Pt(111), a different charge transfer direction was perceived; from Pt(111) to MPc.

- Both FePc and ZnPc were adsorbed on Au(111) and this study demonstrates the effect of the d-orbital filling on the central metal atom of the Pc on the charge transfer at the interface. Fe has unoccupied d orbitals and both HOMO and LUMO of FePc have contributions from the Fe3d, while in Zn, the d-shell is fully filled. This induces hybridization of Fe with Au and results in stronger bond between FePc and the substrate with respect to ZnPc. The FePc film has a higher conductivity, manifested as an absence of coverage-dependent shifts in the core level spectra. The direct interaction of FePc with Au is nicely demonstrated in the appearance of the former LUMO peak just below the Fermi edge.

Beside, FePc and ZnPc which were lying flat on the substrate at the monolayer regime, have different molecular at the thick film. FePc, possessing higher intermolecular interaction in the thick film, holds an upright configuration, while ZnPc molecules keep the flat configuration.

- ZnPc was adsorbed on three substrates; Au(111), Pt(111) and TiO$_2$(110). The interfacial interaction was weaker on Au, compared to the two other surfaces. C1s and N1s spectra from both a monolayer and a thick film of ZnPc on Au(111) showed molecular line profile, whereas monolayer spectra of ZnPc on Pt and TiO$_2$ were strongly disturbed, due to interaction with the substrate. Moreover, ZnPc form a well-ordered monolayer on Au, while on Pt and TiO$_2$ molecules are arranged in different layers already at the ML coverage. Stronger interfacial interaction with Pt and TiO$_2$ also results in inhomogeneous charge transfer and a non-planar configuration for ZnPc. Upon inserting the iodine layer between ZnPc and Pt, this interfacial interaction as well as the inhomogeneity is reduced. The iodine between ZnPc and Au(111) also led to reduction of charge transfer at the interface.

- Adsorption of MgPc on TiO$_2$(110) 1×1 and 1×2-cross-linked illustrated the influence of the surface structure on the molecular configuration. Besides, adsorption on 1×1 led to a 0.25 eV downward band bending at the surface. It creates a charge accumulation layer, with the Fermi level above the conduction band minimum. In 1×2-cross-linked surface, Fermi level is already above CBM, and no further band bending is observed.

- Adsorption of 4TBP on Pt(111) dissociatively breaks the C-H bond, and the molecules are adsorbed with N and the neighboring H-free carbon to Pt. However upon adsorption of 4TBP on Pt(111)-I surfaces, dissociation does not take place. Two different iodine structures were formed at the surface. When 4TBP is adsorbed on Pt-I$\left(\sqrt{3} \times \sqrt{3}\right)$, a competition between 4TBP and iodine to directly bind to Pt(111) was observed, but on Pt-I$\left(\sqrt{7} \times \sqrt{7}\right)$, 4TBP was not in direct contact with Pt(111). Thus 4TBP may affect the adsorption and release in DSSCs.

- 4TBP adsorption on TiO$_2$, demonstrated that oxygen vacancies are favored bond sites for 4TBP at the low coverage. Adsorption of 4TBP on the oxygen vacancies "heal" those sites and the gap state related to these vacancies is significantly reduced. Electrons are transferred to π^* orbitals of the pyridine ring, and as consequence of this charge transfer, the substrate band edge is shifted.

There are a few suggested experiments, related to the work presented in this thesis which can be of interest to be investigated in future.

- Performing experiments on different molecules as dyes, preferably common dyes which are proven to give high efficiency when applied in dye sensitized solar cells. Also studying different substrates and intermediate layers to develop the atomic-level studies closer to the realistic working situation of DSSCs. In order to do so, there might be a need to use high pressure measurements and in liquids.

- Performing X-ray Standing Wave measurements to study the atomic distances from the substrate. Studies done in this thesis demonstrated that characteristics of the charge transfer, the molecular configuration and the electronic structure are influenced by atomic distances.

- Carry out XMCD experiments on transition metal phthalocyanines to further investigate their magnetic properties.

- STM measurements on MPc adsorbed on Au-I$\left(5 \times \sqrt{3}\right)$ and investigate the effect of charge density waves on the MPc adsorption, both molecular configuration and electronic distribution.

Bibliography

[1] L.R. Milgrom, *The Colours of Life-An Introduction to the Chemistry of Porphyrins and Related Copmpounds* (Oxford University Press, New York, 1997).

[2] O.L. Kaliya, E.A. Lukyanet, and G.N. Vorozhtsov, J. Porphyr. Phthalocyanines **3**, 592 (1999).

[3] C.K. Mathews, K.E. van Holde, and K.G. Ahren, Biochemistry, (2000).

[4] F. Zhao, F. Harnisch, U. Schröder, F. Scholz, P. Bogdanoff, and I. Herrmann, Electrochem. Commun. **7**, 1405 (2005).

[5] L. Zhang, J. Zhang, D.P. Wilkinson, and H. Wang, J. Power Sources **156**, 171 (2006).

[6] G. Lalande, G. Faubert, R. Cote, G. D, J.P. Dolelet, L.T. Weng, and P. Bertrand, J. Power Sources **3**, 227 (1996).

[7] G. de la Torre, C.G. Claessens, and T. Torres, Chem. Comm **20**, (2007).

[8] J. Yuan, J. Zhang, J. Wang, X. Yan, D. Yan, and W. Xu, Appl. Phys. Lett. **82**, 3967 (2003).

[9] G. Gu, G. Parthasarathy, and S.R. Forrest, Appl. Phys. Lett. **74**, 305 (1999).

[10] L.S. Hung and C.W. Tang, Appl. Phys. Lett. **74**, 3209 (1999).

[11] D. Hohnholz, S. Steinbrecher, and M. Hanack, J. Mol. Struct. **521**, 231 (2000).

[12] M.E. Wieder, D.C. Hone, M.J. Cook, M.M. Handsley, J. Gavrilovic, and D.A. Russell, Photochem. Photobiol. **5**, 727 (2006).

[13] C.M. Allen, W.M. Sharman, and J.E. Van Lier, J. Porphyrins Phthalocyanines **5**, 2001 (2001).

[14] B. Bott and T. Jones, Sens. Actuator **5**, 43 (1984).

[15] S. Wring, J. Hart, and B. Birch, Analyst **114**, 11 (1989).

[16] S. Riad, Thin Solid Films **370**, 253 (2000).

[17] C.G. Claessens, U. Hahn, and T. Torres, Chem. Rec. **8**, 75 (2008).

[18] T. Abe, K. Nagai, K. Sekimoto, A. Tajiri, and T. Norimatsu, Electrochem. Commun **7**, 1129 (2005).

[19] T.S. Ellis, K.T. Park, S.L. Hulbert, M.D. Ulrich, and J.E. Rowe, J. Appl. Phys. **95**, 982 (2004).

[20] Y. Naitoh, T. Matsumoto, K. Sugiura, Y. Sakata, and T. Kawai, Surf. Sci **487**, L534 (2001).

[21] S. Yu, S. Ahmadi, C. Sun, P.T.Z. Adibi, W. Chow, A. Pietzsch, and M. Göthelid, J. Chem. Phys. **136**, 154703 (2012).

[22] L. Zhang, H. Peisert, I. Biswas, M. Knupfer, D. Batchelor, and T. Chassé, Surf. Sci. **596**, 98 (2005).

[23] S. Ahmadi, M.N. Shariati, S. Yu, and M. Göthelid, J. Chem. Phys. **137**, 084705 (2012).

[24] M.T. Akada and H.T. Ada, Jpn. J. Appl. Phys. **44**, 5332 (2005).

[25] I. Biswas, H. Peisert, M. Nagel, M.B. Casu, S. Schuppler, P. Nagel, E. Pellegrin, and T. Chassé, J. Chem. Phys. **126**, 174704 (2007).

[26] Z.H. Cheng, L. Gao, Z.T. Deng, Q. Liu, N. Jiang, X. Lin, X.B. He, S.X. Du, and H.J. Gao, J. Phys. Chem. C **111**, 2656 (2007).

[27] I. Chizhov, G. Scoles, and A. Kahn, Langmuir **16**, 4358 (2000).

[28] A. Cossaro, L. Floreano, R. Gotter, A. Morgante, D. Cvetko, G. Bavdek, F. Evangelista, and A. Ruocco, J. Phys. Chem. B **108**, 14671 (2004).

[29] F. Evangelista, A. Ruocco, V. Corradini, M.P. Donzello, C. Mariani, and M.G. Betti, Surf. Sci **531**, 123 (2003).

[30] Y. Fu, S. Ji, X. Chen, X. Ma, R. Wu, C. Wang, W. Duan, X. Qiu, B. Sun, P. Zhang, J. Jia, and Q. Xue, Phys. Rev. Lett. **99**, 1 (2007).

[31] L. Gao, W. Ji, Y.B. Hu, Z.H. Cheng, Z.T. Deng, Q. Liu, N. Jiang, X. Lin, W. Guo, S.X. Du, W.A. Hofer, X.C. Xie, and H. Gao, Surf. Sci. **106402**, 2 (2007).

[32] L. Grządziel, M. Krzywiecki, H. Peisert, T. Chassé, and J. Szuber, Thin Solid Films **519**, 2187 (2011).

[33] S. Yu, S. Ahmadi, C. Sun, K. Schulte, A. Pietzsch, F. Hennies, M. Zuleta, and M. Göthelid, J. Phys. Chem. C **115**, 14969 (2011).

[34] B. Brena, P. Palmgren, K. Nilson, S. Yu, F. Hennies, B. Agnarsson, A. Önsten, M. Månsson, and M. Göthelid, Surf. Sci. **603**, 3160 (2009).

[35] S. Dick and H. Peisert, J. Appl. Phys. 1 (2005).

[36] F. Evangelista, R. Gotter, N. Mahne, S. Nannarone, A. Ruocco, and P. Rudolf, J. Phys. Chem. C **112**, 6509 (2008).

[37] A. Gerlach, F. Schreiber, S. Sellner, H. Dosch, I. Vartanyants, B. Cowie, T.-L. Lee, and J. Zegenhagen, Phys. Rev. B **71**, 205425 (2005).

[38] S. Yu, S. Ahmadi, P. Palmgren, F. Hennies, M. Zuleta, and M. Göthelid, J. Phys. Chem. C **113**, 13765 (2009).

[39] P. Palmgren, S. Yu, F. Hennies, K. Nilson, B. Åkermark, and M. Göthelid, J. Chem. Phys. **129**, 074707 (2008).

[40] C. Isvoranu, B. Wang, K. Schulte, E. Ataman, J. Knudsen, J.N. Andersen, M.L. Bocquet, and J. Schnadt, J. Phys Condens. Matter **22**, 472002 (2010).

[41] C. Isvoranu, B. Wang, E. Ataman, K. Schulte, J. Knudsen, J.N. Andersen, M. Bocquet, and J. Schnadt, J. Chem. Phys. **134**, 114710 (2011).

[42] C. Isvoranu, B. Wang, E. Ataman, K. Schulte, J. Knudsen, J.N. Andersen, M.-L. Bocquet, and J. Schnadt, J. Phys. Chem. C **115**, 20201 (2011).

[43] C. Isvoranu, B. Wang, E. Ataman, J. Knudsen, K. Schulte, J.N. Andersen, M.-L. Bocquet, and J. Schnadt, J. Phys. Chem. C **115**, 24718 (2011).

[44] C. Isvoranu, J. Knudsen, E. Ataman, K. Schulte, B. Wang, M.-L. Bocquet, J.N. Andersen, and J. Schnadt, J. Chem. Phys. **134**, 114711 (2011).

[45] M. Grätzel, J. Photochem. Photobiol. C **4**, 145 (2003).

[46] M.K. Nazeeruddin, A. Kay, E. Muller, P. Liska, N. Vlachopoulos, and M. Grätzel, J. Am. Chem. Soc. **115**, 6382 (1993).

[47] S. Hufner, *Photoelectron Spectroscopy* (Springer Verlag, Berlin, 2003).

[48] K.A.I. Siegbahn, Pure Appl. Chem. **48**, 77 (1976).

[49] J.J. Yeh and I. Lindau, At. Data. Nucl. Data. Tables. **32**, 1 (1985).

[50] M.P. Seah and W.A. Dench, Surf. Interface Anal. **1**, 2 (1979).

[51] J.N. Andersen and C.-O. Almbladh, Condens. Matter. **13**, 11267 (2001).

[52] G. Binnig, H. Rohrer, C. Gerber, and E. Weibel, Appl. Phys. Lett. **40**, 178 (1982).

[53] G. Binnig, H. Rohrer, C. Gerber, and E. Weibel, Phys. Rev. Lett **49**, 57 (1982).

[54] G. Binnig, H. Rohrer, C. Gerber, and E. Weibel, Phys. Rev. Lett **50**, (1983).

[55] D. Drakova, Rep. Prog. Phys. **205**, 205 (2001).

[56] H. Lüth, *Solid Surfaces, Interfaces and Thin Films* (Springer Verlag, Berlin, 2001).

[57] C. Stadler, S. Hansen, F. Pollinger, C. Kumpf, E. Umbach, T.-L. Lee, and J. Zegenhagen, Phys. Rev. B **74**, 035404 (2006).

[58] J.D. Baran, J.A. Larsson, R.A.J. Wooley, Y. Cong, P.J. Moriarty, A.A. Cafolla, K. Schulte, and V.R. Dhanak, Phys. Rev. B **81**, 1 (2010).

[59] M.-S. Liao and S. Scheiner, J. Chem. Phys. **114**, 9780 (2001).

[60] T. Nishi, K. Kanai, Y. Ouchi, M.R. Willis, and K. Seki, Proc. Int. Symp. Super-Functionality Org. Devices **6**, 35 (n.d.).

[61] H. Peisert, T. Chasse, and A. Petershans, J. Phys. Chem. Lett **112**, 5703 (2008).

[62] M.G. Betti, P. Gargiani, R. Frisenda, R. Biagi, A. Cossaro, A. Verdini, L. Floreano, and C. Mariani, J. Phys. Chem. C **114**, 21638 (2010).

[63] F. Petraki, H. Peisert, F. Latteyer, U. Aygül, A. Vollmer, and T. Chassé, J. Phys. Chem. C **115**, 21334 (2011).

[64] F. Petraki, H. Peisert, I. Biswas, and T. Chassé, J. Phys. Chem. C **114**, 17638 (2010).

[65] F. Petraki, H. Peisert, and U. Aygul, J. Phys. Chem. C **116**, (2012).

[66] F. Petraki, V. Papaefthimiou, and S. Kennou, J. P. C. S. **135**, 1 (2005).

[67] J. Xiao and P.A. Dowben, J. Phys. Condens. Matter **21**, 052001 (2009).

[68] H. Peisert, D. Kolacyak, and T. Chassé, J. Phys. Chem. C **113**, 19244 (2009).

[69] F. Sedona, M. Di Marino, D. Forrer, A. Vittadini, M. Casarin, A. Cossaro, L. Floreano, A. Verdini, and M. Sambi, Nat. Mater. **11**, 970 (2012).

[70] J. Bartolomé, F. Bartolomé, L.M. García, G. Filoti, T. Gredig, C.N. Colesniuc, I.K. Schuller, and J.C. Cezar, Phys. Rev. B **81**, 195405 (2010).

[71] X. Lu, K. Hipps, X. Wang, and U. Mazur, J. Phys. Chem. B **5647**, 5391 (1996).

[72] P. Gargiani, M. Angelucci, C. Mariani, and M.G. Betti, Phys. Rev. B **81**, 1 (2010).

[73] I. Kröger, B. Stadtmüller, C. Stadler, J. Ziroff, M. Kochler, A. Stahl, F. Pollinger, T.-L. Lee, J. Zegenhagen, F. Reinert, and C. Kumpf, New. J. Phys. **12**, 083038 (2010).

[74] K. Nilson, J. Åhlund, M. Shariati, E. Göthelid, P. Palmgren, J. Schiessling, S. Berner, N. Mårtensson, and C. Puglia, J. Phys. Chem. C **114**, 12166 (2010).

[75] J. Åhlund, J. Schnadt, K. Nilson, E. Göthelid, J. Schiessling, F. Besenbacher, N. Mårtensson, and C. Puglia, Surf. Sci. **601**, 3661 (2007).

[76] C. Stadler, S. Hansen, I. Kröger, C. Kumpf, and E. Umbach, Nat. Phys. **5**, 153 (2009).

[77] G. Schlichthörl, S. Huang, J. Sprague, and J. Frank, J. Phys. Chem. B **5647**, 8141 (1997).

[78] G. Boschloo, L. Häggman, and A. Hagfeldt, J. Phys.Chem. B **110**, 13144 (2006).

[79] C. Shi, S. Dai, K. Wang, X. Pan, F. Kong, and L. Hu, Vib. Spectrosc. **39**, 99 (2005).

[80] J. V. Barth, H. Brune, G. Ertl, and R.J. Behm, Phys. Rev. B **42**, 9307 (1990).

[81] L. Huang, P. Zeppenfeld, S. Horch, and G. Comsa, J. Chem. Phys. **107**, 585 (1997).

[82] B.M. Ocko, G.M. Watson, and J. Wang, J. Phys. Chem. **98**, 897 (1994).

[83] S.A. Cochran and H.H. Farrell, Surf. Sci **95**, 359 (1980).

[84] Z. V. Zheleva, V.R. Dhanak, and G. Held, Phys. Chem. Chem. Phys **12**, 10754 (2010).

[85] K. Doll and N.M. Harrison, J. Chem. Phys. Lett **317**, 282 (2000).

[86] A.G. Shard, C. Ton-That, P.A. Campbell, and V.R. Dhanak, Phys. Rev. B **70**, 155409 (2004).

[87] X. Gao and M.J. Weaver, J. Am. Chem. Soc. **114**, 8544 (1992).

[88] B.C. Bravo, S.L. Michelhaugh, and M.P. Soriaga, J. Phys. Chem. **95**, 5245 (1991).

[89] M. N, U. Starke, A. Barbieri, R. Döll, K. Heinz, M.A. Van Hove, and G.A. Somorjai, Surf. Sci **325**, 207 (1995).

[90] S.K. Jo and J.M. White, Surf. Sci **261**, 111 (1992).

[91] U. Diebold, Surf. Sci. Rep. **48**, 53 (2003).

[92] V.E. Henrich and P.A. Cox, *The Surface Science of Metal Oxides* (Cambridge University Press, Cambridge, 1994).

[93] M. Göthelid, S. Yu, S. Ahmadi, C. Sun, and M. Zuleta, INT. J. PHOTOENERGY. **2011**, 1 (2011).

[94] W. Chen, C. Huang, X.Y. Gao, L. Wang, C.G. Zhen, D. Qi, S. Chen, H.L. Zhang, K.P. Loh, Z.K. Chen, A. Thye, and S. Wee, J. Phys. Chem. B **110**, 26075 (2006).

[95] W. Brütting, *Physics of Organic Semiconductors* (n.d.), pp. Wiley–VCH, Germany.

[96] W. Gao and A. Kahn, Org. Electron. **3**, 53 (2002).

[97] L. Chen, L. Yang, Z. Yang, M. Shi, M. Wang, H. Chen, W. Zhang, and F. Xu, J. Phys. Chem. C **113**, 17160 (2009).

[98] X. Lu and K.W. Hipps, J. Phys. Chem. B **101**, 5391 (1997).

[99] X. Lu, K.W. Hipps, X.D. Wang, and U. Mazur, J. Am. Chem. Soc. **118**, 7197 (1996).

[100] B.M. Barry and E.G. Gillan, Chem. Matter. **21**, 4454 (2009).

[101] G. Mattioli, F. Filippone, P. Giannozzi, R. Caminiti, and A. Amore Bonapasta, Phys. Rev. Lett **101**, 126805 (2008).

[102] L. Giovanelli, P. Vilmercati, C. Castellarin-Cudia, J.-M. Themlin, L. Porte, and A. Goldoni, J. Chem. Phys. **126**, 044709 (2007).

[103] W. Chen, H. Huang, S. Chen, Y.L. Huang, X.Y. Gao, and A.T.S. Wee, Chem. Mater. **20**, 7017 (2008).

[104] E. Herceg, J. Jones, K. Mudiyanselage, and M. Trenary, Surf. Sci. **600**, 4563 (2006).

[105] O. Björneholm, A. Nilsson, H. Tillborg, P. Bennich, A. Sandell, B. Hernnäs, C. Puglia, and N. Mårtensson, Surf. Sci **6028**, L983 (1994).

[106] E. Janin, S. Ringler, J. Weissenrieder, T. Åkermark, U.O. Karlsson, M. Göthelid, D. Nordlund, and H. Ogasawara, Surf. Sci. **485**, (2001).

[107] S. Suzuki, H. Onishi, T. Sasaki, K. Fukui, and Y. Iwasawa, Catal. Lett. **54**, 177 (1998).

Abbreviations

4TBP	4-Tert-Butyl Pyridine
CB	Conduction Band
DFT	Density Functional Theory
HOMO	Highest Occupied Molecular Orbital
LEED	Low-Energy Electron Diffraction
LUMO	Lowest Unoccupied Molecular Orbital
ML	Monolayer
NEXAFS	Near-Edge X-ray Absorption Fine Structure
Pc	Phthalocyanine
RT	Room Temperature
STM	Scanning Tunneling Microscopy
TF	Thick Film
UHV	Ultra High Vacuum
UV	Ultra-violet
VB	Valence band
VT	Variable Temperature
XAS	X-ray Absorption Spectroscopy
XPS	X-ray Photoelectron Spectroscopy

Summary of contributions

I. **Sareh Ahmadi**, Nina Shariati, Shun Yu and Mats Göthelid, "Molecular layers of ZnPc and FePc on Au(111) surface: Charge transfer and chemical interaction", *J. Chem. Phys.* 137 **(2012)** 084705

Contributions: Planned the experiments. Performed sample preparation, all measurements and data analysis. Wrote the major part of the manuscript.

II. **Sareh Ahmadi**, Shun Yu, Markus Soldemo, Chenghua Sun and Mats Göthelid, "Reduced Au-MPc hole injection barrier by an intermediate iodine layer", Submitted to *J. Phys. Chem. C.*

Contributions: Planned and performed the experiment, performed data analysis and interpretation. Wrote the major part of the manuscript.

III. **Sareh Ahmadi**, Björn Agnarsson, Ieva Bidermane, Bastian. M. Wojek, Quentin Noel and Mats Göthelid, "Effect of the iodine on the site-dependent charge transfer at the Pt(111)-ZnPc interface", Submitted to *New. J. Phys.*

Contributions: Planned and performed the experiment. Analyzed data and wrote the manuscript.

IV. Shun Yu, **Sareh Ahmadi**, Chenghua Sun, Pooya Tabib Zadeh Adibi, Winnie Chow, Annette Pietzsch and Mats Göthelid, "Inhomogeneous charge transfer within monolayer zinc phthalocyanine adsorbed on $TiO_2(110)$", *J. Chem. Phys.* 136, **(2012)** 154703

Contributions: Took part in the experiment and contributed to the analysis and interpretation of data. Contributed to the manuscript.

V. **Sareh Ahmadi**, Shun Yu, Markus Soldemo, Marcelo Zuleta, Pål Palmgren and Mats Göthelid, "Charge transfer and band bending on $TiO_2(110)$-MgPc", Submitted to *J. Phys. Chem. C.*

Contributions: Performed sample preparation, all measurements and data analysis. Wrote the major part of the manuscript.

VI. **Sareh Ahmadi**, Ieva Bidermane, Quentin Noel, Chenghua Sun and Mats Göthelid, "Dissociative bonding of 4-tert-butyl pyridine to Pt(111) and surface passivation by iodine", *manuscript.*

Contributions: Planned and performed the experiment. Performed data analysis and data interpretation. Wrote the major part of the manuscript.

VII.   Shun Yu, Sareh Ahmadi, Chenghua Sun, Pål Palmgren, Franz Hennies, Marcelo Zuleta, Mats Göthelid, "4-tert-butyl pyridine bond site and band bending on $TiO_2(110)$", *J. Phys. Chem. C*, (**2010**), 114, 2315-2320

Contributions: Took part in the experiment and contributed to the analysis and interpretation of data. Contributed to the manuscript.

Manuscripts